Inferring Cirrus Size Distributions through Satellite Remote Sensing and Microphysical Databases

DAVID L. MITCHELL

Desert Research Institute, Reno, Nevada

ROBERT P. d'ENTREMONT

Atmospheric and Environmental Research, Inc., Lexington, Massachusetts

R. PAUL LAWSON

SPEC, Inc., Boulder, Colorado

(Manuscript received 19 March 2009, in final form 16 October 2009)

ABSTRACT

Since cirrus clouds have a substantial influence on the global energy balance that depends on their microphysical properties, climate models should strive to realistically characterize the cirrus ice particle size distribution (PSD), at least in a climatological sense. To date, the airborne in situ measurements of the cirrus PSD have contained large uncertainties due to errors in measuring small ice crystals ($D \lesssim 60$ μm). This paper presents a method to remotely estimate the concentration of the small ice crystals relative to the larger ones using the 11- and 12-μm channels aboard several satellites. By understanding the underlying physics producing the emissivity difference between these channels, this emissivity difference can be used to infer the relative concentration of small ice crystals. This is facilitated by enlisting temperature-dependent characterizations of the PSD (i.e., PSD schemes) based on in situ measurements.

An average cirrus emissivity relationship between 12 and 11 μm is developed here using the Moderate Resolution Imaging Spectroradiometer (MODIS) satellite instrument and is used to "retrieve" the PSD based on six different PSD schemes. The PSDs from the measurement-based PSD schemes are compared with corresponding retrieved PSDs to evaluate differences in small ice crystal concentrations. The retrieved PSDs generally had lower concentrations of small ice particles, with total number concentration independent of temperature. In addition, the temperature dependence of the PSD effective diameter D_e and fall speed V_f for these retrieved PSD schemes exhibited less variability relative to the unmodified PSD schemes. The reduced variability in the retrieved D_e and V_f was attributed to the lower concentrations of small ice crystals in the retrieved PSD.

1. Introduction

The measurement of small ice crystals ($D < 60$ μm) has been a controversial issue in the atmospheric sciences community largely because their concentrations may be partially due to the shattering of larger ice particles at the inlet of the probes that measure them, resulting in artifact ice crystals. Depending on the in situ measurements one uses, these small ice crystals may affect cirrus cloud optical depth by a factor of 2 (McFarquhar et al. 2007). The concentration of these small crystals relative to larger ice particles is critical to climate prediction (Mitchell et al. 2008) since this affects the overall ice sedimentation rate of the ice particle size distribution (PSD). Through their impact on ice fall speeds, their relative concentration affects the cirrus cloud feedback and climate sensitivity (the equilibrium change in global mean surface temperature) in global circulation models (GCMs). Sanderson et al. (2008) show that next to the entrainment coefficient, the ice fall speed has the greatest impact on climate sensitivity in thousands of perturbed physics GCM experiments.

Corresponding author address: Dr. David L. Mitchell, Desert Research Institute, Division of Atmospheric Sciences, Reno, NV 89512-1095.
E-mail: mitch@dri.edu

DOI: 10.1175/2009JAS3150.1

The measured concentrations of small ice crystals are often orders of magnitude greater than that of the larger particles (McFarquhar and Heymsfield 1997; Ivanova et al. 2001; Lawson et al. 2006a; Garrett et al. 2005). The instruments used to measure the concentrations of small ice crystals include, but are not limited to, the ice particle replicator (Hallett 1976), the Video Ice Particle Sampler (VIPS) (McFarquhar and Heymsfield 1996), the Forward Scattering Spectrometer Probe (FSSP) (Knollenberg 1981) and the Cloud Aerosol Spectrometer (CAS) (Baumgardner et al. 2001). The FSSP and the CAS have an inlet tube in which ice particle shattering could easily occur. The replicator and VIPS do not have an inlet tube but their collection efficiency varies as a function of particle size.

Recent progress in instrument design and signal processing has resulted in new probes for measuring cloud PSDs (Baumgardner et al. 2001; Lawson et al. 2006b). Evidence of ice artifact production resulting from shattering is given in Field et al. (2003), McFarquhar et al. (2007), Heymsfield (2007), and Jensen et al. (2009). Evidence that the FSSP can measure realistic number concentrations is given in Ivanova et al. (2001) and Gayet et al. (2006).

In view of these types of conflicting results regarding the measurements of small ice crystal concentrations, this study addresses this issue using results derived from in situ measurements and from satellite remote sensing. A new satellite remote sensing technique has been developed that uses parameterized results from aircraft measurements to help characterize the larger ice particles ($D > 60$ μm). That is, in situ measurements of ice particle size distributions are parameterized by temperature and ice water content (IWC), henceforth referred to as PSD schemes. To characterize the smaller ice crystals of the PSD, the effective cirrus cloud absorption optical depth ratio obtained from satellite measured radiances at 12 and 11 μm is used. Based on several satellite remote sensing studies of midlatitude and tropical cirrus, the ratio appears to have climatological significance, and so does the relative concentration of small ice crystals estimated from this ratio. Combining the satellite-inferred information with the PSD estimate for the larger ice particles yields the entire parameterized PSD for a given IWC. While satellite measurements have their own uncertainties, the problem of artifact small ice particles from shattering is avoided using this approach.

Theory concerning ice particle–radiation interactions is described in section 2. Section 3 describes two retrieval methods for the cirrus absorption optical depth ratio and microphysics. The results are presented and discussed in section 4, and a summary is given in section 5.

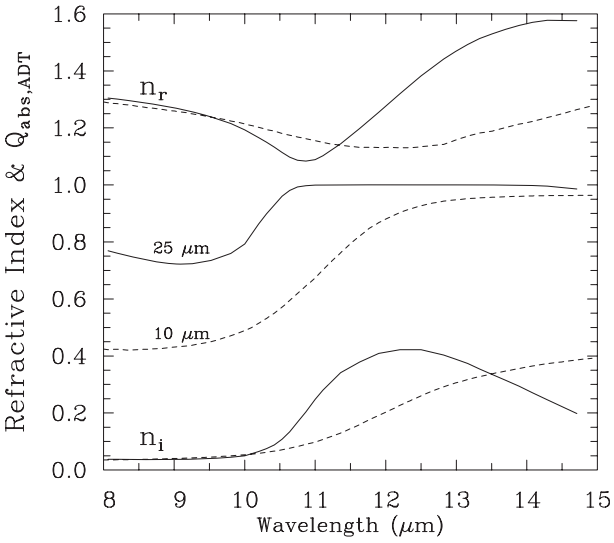

FIG. 1. Solid (dashed) curves correspond to ice (liquid water), showing the (top) real and (bottom) imaginary refractive index. The two middle curves show the ADT absorption efficiency for an ice crystal having an effective size of a 25- and a 10-μm cloud droplet, where absorption occurs only over the particle cross section. See text for details.

2. Radiation theory for cloud particles

The modified anomalous diffraction approximation (MADA) (Mitchell et al. 1996, 2006a; Mitchell 2000, 2002) is used to treat ice cloud optical properties in the retrieval algorithm. With MADA, extinction and absorption are expressed in terms of the parameters of a gamma function PSD and the representative measured mass–dimension and projected area–dimension power law relationships. This dependence allows us to estimate PSD information from satellite radiances.

To evaluate the relative concentration of small ice crystals in cirrus clouds, we use the cloud emissivity difference retrieved in the 12- and 11-μm bands that are a common component of many environmental satellite sensors. To understand how this is possible, the absorption processes involved and how they differ between liquid water and ice particles need to be understood. These fundamental insights are illustrated in Fig. 1, where the real and imaginary refractive index (n_r and n_i) for bulk ice and water are plotted against wavelength (refractive indexes from Warren and Brandt 2008; Downing and Williams 1975). Also plotted is the cloud particle absorption efficiency, $Q_{\rm abs}$, which is given by the simple anomalous diffraction theory (ADT) described in Mitchell and Arnott (1994):

$$Q_{\rm abs,ADT} = 1 - \exp(-4\pi n_i d_e/\lambda), \qquad (1)$$

where λ is wavelength and particle effective size d_e is defined as $d_e = m/\rho A_p$ where m is particle mass, ρ is bulk

density of water or ice, and A_p is particle cross section or projected area. The $Q_{\text{abs,ADT}}$ values correspond to a cloud droplet and ice particle d_e of 10 and 25 μm, respectively, with 10 μm being typical for water clouds. In the absence of very high concentrations of small ice crystals, an ice particle d_e of 25 μm is considered small, with more than about 90% of the PSD projected area residing with larger particles (Jensen et al. 2009). Thus, for most cirrus ice particles, for wavelengths greater than 10.5 μm, $Q_{\text{abs,ADT}} \approx 1.0$, meaning that all radiation incident upon the particle's cross section is absorbed. Under such conditions we can apply the zero-scattering approximation for cloud emissivity ε:

$$\varepsilon = 1 - \exp(-\tau_{\text{abs}}/\cos\theta) = 1 - \exp(-\overline{Q}_{\text{abs}} P_t \Delta z/\cos\theta), \tag{2}$$

where τ_{abs} is absorption optical depth, θ is satellite viewing angle, $\overline{Q}_{\text{abs}} = \beta_{\text{abs}}/P_t$, β_{abs} = absorption coefficient, P_t is PSD projected area, and Δz is cloud depth. If $\overline{Q}_{\text{abs}}$ in (2) is approximated as $\overline{Q}_{\text{abs,ADT}}$ using (1), then $\varepsilon(11\ \mu\text{m}) \approx \varepsilon(12\ \mu\text{m})$. Thus, there must be an additional process other than the Beer's law absorption represented in ADT that is responsible for the observed differences between $\varepsilon(11\ \mu\text{m})$ and $\varepsilon(12\ \mu\text{m})$. This other process is referred to as wave resonance or photon tunneling. In Mitchell (2000), the maximum tunneling contribution is shown to be directly proportional to n_r. In Fig. 1, the solid curves refer to ice and the ice n_r curve is seen to increase almost linearly between 11 and 13 μm, implying a quasi-linear absorption contribution from tunneling. Although previous literature has credited n_i for the cirrus cloud emissivity difference between $\varepsilon(11\ \mu\text{m})$ and $\varepsilon(12\ \mu\text{m})$, it is actually n_r that is responsible, with the emissivity difference due to differences in tunneling contributions to absorption.

The dashed curves in Fig. 1 refer to liquid water refractive indexes and $Q_{\text{abs,ADT}}$ for a cloud droplet having $d_e = 10$ μm. It is seen for water that tunneling does not contribute to the difference between $\varepsilon(11\ \mu\text{m})$ and $\varepsilon(12\ \mu\text{m})$ since n_r is almost constant over those wavelengths. The rapid change in $Q_{\text{abs,ADT}}$ between 11 and 12 μm shows that it is Beer's law absorption based on n_i that is responsible for the emissivity differences in liquid water clouds.

We now show that small ice crystals can be evaluated using the properties of photon tunneling or wave resonance. Photon tunneling can be described as the process by which radiation beyond the physical cross section of a particle is either absorbed or scattered outside the forward diffraction peak. As shown in Mitchell (2000) and Mitchell et al. (2006a), tunneling is strongest when

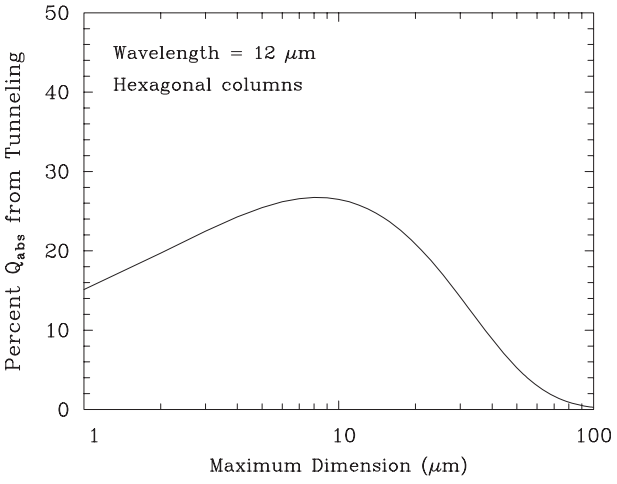

FIG. 2. Size dependence of the photon tunneling contribution (i.e., wave resonance) to the absorption efficiency of a hexagonal column for a wavelength of 12 μm.

(i) the wavelength and the effective size of the particle are comparable,
(ii) the particle is spherical or quasi-spherical, and
(iii) the real part of the refractive index is relatively large.

Attribute (i) is illustrated in Fig. 2 for a wavelength of 12 μm, where it is seen that the absorption contribution from tunneling is significant for hexagonal columns less than 60 μm and can account for 20% or more of the absorption efficiency. This tunneling contribution was calculated from Eq. (10) in Mitchell (2000). Since the shape of ice crystals becomes more spherical as their size decreases (Korolev and Isaac 2003), their tunneling contribution is enhanced via attribute (ii). Finally, the wavelength dependence of tunneling in Fig. 1 suggests the difference in absorption between 12 and 11 μm, or the 12/11-μm absorption efficiency ratio, defined as β, might be a useful signal for detecting small ice crystals.

The operating principle of this remote sensing method is further illustrated in Fig. 3. The solid curve shows $\overline{Q}_{\text{abs}}$ for a bimodal size distribution of quasi-spheres (droxtals) in the small mode and bullet rosettes in the large mode. The dashed curve is for the large-mode rosettes only. The $\overline{Q}_{\text{abs}}$ for wavelengths more than 11 μm are greater for the complete PSD owing to tunneling. The reason $\overline{Q}_{\text{abs}}$ is greater between 11 and 13 μm when the full PSD is used is because of the first two factors listed above regarding small ice crystals, and $\overline{Q}_{\text{abs}}(12\ \mu\text{m}) > \overline{Q}_{\text{abs}}(11\ \mu\text{m})$ because of the third factor $[n_r(12\ \mu\text{m}) > n_r(11\ \mu\text{m})]$. Since tunneling is only a measure of the small mode and the ratio $\overline{Q}_{\text{abs}}(12\ \mu\text{m})/\overline{Q}_{\text{abs}}(11\ \mu\text{m})$, or β, is determined from tunneling, this ratio serves as a measure of the small mode of the cirrus PSD. These

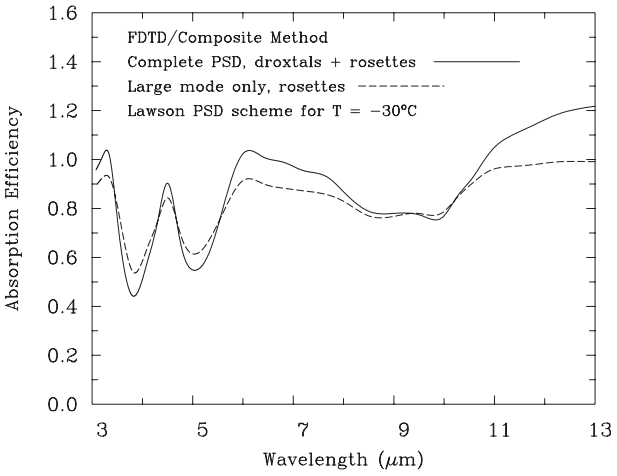

FIG. 3. Absorption efficiencies for a bimodal size distribution (solid) and the same PSD but without the small crystal mode (dashed). The difference in the curves between 11 and 13 μm is due only to tunneling.

calculations are based on the optical property database given in Yang et al. (2005), but the same result is given by MADA.

MADA is unique in that it is analytically formulated in terms of explicitly parameterized scattering/absorption processes. As described in Mitchell et al. (2006a), tunneling efficiencies (T_e) for various ice crystal shapes were determined by comparisons between MADA and finite-difference time-domain (FDTD) calculations and were parameterized as a function of ice particle shape and large mode $\overline{D}$. Based on Cloud Particle Imager (CPI) ice crystal morphology measurements in synoptic cirrus, 53% of the small ice crystals were assumed to be quasi-spherical ($T_e = 1.0$), 31% compact-irregular ($T_e = 0.70$), and 16% budding bullet rosettes ($T_e = 0.70$). At these small sizes ($D < 40$ μm), most ice crystal shapes exhibit aspect ratios close to 1.0 and thus have relatively high tunneling efficiencies between 0.70 and 1.00. Tunneling contributions from the larger ice particles was negligible regardless of T_e owing to the size dependence of tunneling (Fig. 2).

3. Estimating small ice crystal concentrations

a. Microphysical framework

Our challenge is to estimate the relative concentration of small-to-larger ice particles in a size distribution. A bimodal PSD framework is adopted here, where each mode of the PSD is described as a gamma function of the form

$$N(D) = N_o D^{\nu} \exp(-\lambda D), \quad (3)$$

where λ is the slope parameter, ν is the dispersion or width parameter, and N_o relates the other two parameters to the PSD (or mode) number concentration N or IWC. While our objective is to estimate the complete PSD for a given IWC, each PSD mode is described by the three terms in (3). With six PSD terms, there are more unknowns than we can infer from two measured radiances. The PSD terms that we cannot infer from satellite radiances are estimated from a temperature-dependent PSD scheme (derived from in situ measurements) that provides a bimodal PSD estimate given a satellite-retrieved cloud temperature and an assumed IWC. Since the measurement uncertainties associated with the larger ice particles are expected to be less than the small crystal uncertainties, we approximate the large-mode mean size from temperature (e.g., Ryan 1996; Platt 1997; Ivanova et al. 2001; Donovan 2003; Field et al. 2007). For reasons given in section 2, the relative contribution of the small ($D < 60$ μm) ice crystals can be estimated from satellite radiances. By combining the PSD scheme based on in situ measurements of the larger ice particles with radiance measurements that are sensitive to the small PSD mode, an estimate of the complete PSD (bimodal or monomodal) can be retrieved for a given IWC. The only restriction on the choice of IWC is that it should not yield an ice water path (IWP) that causes $\varepsilon(11\ \mu\text{m}) \rightarrow 1.0$ (i.e., a blackbody). We assumed IWC = 10 mg m^{-3} and IWP = 15 g m^{-2}.

A salient feature of this study is the ability to couch the derived cirrus PSDs in a "climatological context." Parameterizations of PSDs from six studies described in the literature are examined using satellite radiance measurements of cirrus (explained in section 3b). The PSDs described in Lawson et al. (2006a) were parameterized as described in the appendix. The other PSD schemes were extracted from Ivanova et al. (2001), Donovan (2003), Heymsfield (2003), Ivanova (2004), and Schmitt and Heymsfield (2009). The Donovan scheme is based on lidar–radar ground-based remote sensing.

The Heymsfield (2003) and Schmitt and Heymsfield (2009) PSD schemes are monomodal whereas the others are formulated as bimodal. The modified gamma functions in Donovan (2003) were reformulated as gamma functions. A given PSD scheme provides an initial estimate via cloud temperature for the large-mode slope parameter or mean size. It also defines ν for the large and small mode and λ for the small mode. The satellite-measured radiances are used to estimate the small-mode IWC (related to the parameter N_o) and sometimes to modify the large-mode λ. For the monomodal PSD schemes, we use Ivanova et al. (2001) to define the small-mode ν and λ in the retrieval algorithm.

b. Effective absorption optical depth ratio

To estimate the complete PSD we use the 12-to-11 μm effective absorption optical depth ratio, or β_{eff}, where β_{eff} is calculated from satellite measured effective emissivities (i.e., based on the zero-scattering approximation) of semitransparent cirrus. The relative concentration of small ice crystals is then estimated from β_{eff}. To appraise these concentrations in a climatological context, the β_{eff} retrievals should be sufficiently extensive.

The absorption optical depth ratio is equivalent to the absorption efficiency ratio $\overline{Q}_{\text{abs}}$ (12 μm)/$\overline{Q}_{\text{abs}}$(11 μm) and is independent of IWC. To account for scattering effects, Parol et al. (1991) recommend using an effective absorption efficiency ratio that is equivalent to β_{eff}, where

$$\beta_{\text{eff}} = \overline{Q}_{\text{abs,eff}}(12\,\mu\text{m})/\overline{Q}_{\text{abs,eff}}(11\,\mu\text{m}) \tag{4}$$

and

$$\overline{Q}_{\text{abs,eff}} = \overline{Q}_{\text{abs}}(1 - \omega_o g)/(1 - \omega_o), \tag{5}$$

where g is an asymmetry parameter and ω_o is single scattering albedo of the PSD. When all radiation is scattered in the forward direction (approached in nonscattering conditions), $g = 1$ and $\overline{Q}_{\text{abs,eff}} = \overline{Q}_{\text{abs}}$ in the PSD retrieval algorithm; β_{eff} is calculated from (4) using the g parameterization given in Yang et al. (2005). In the effective emissivity satellite retrieval, β_{eff} is calculated as (Inoue 1985)

$$\varepsilon_{\text{eff}}(12\,\mu\text{m}) = 1 - [1 - \varepsilon_{\text{eff}}(11\,\mu\text{m})]^{\beta_{\text{eff}}}. \tag{6}$$

SATELLITE RETRIEVAL OF β_{EFF}

Using the Advanced Very High Resolution Radiometer (AVHRR) channels 4 (10.5–11.5 μm) and 5 (11.5–12.5 μm) aboard the polar-orbiting satellite *NOAA-7*, Inoue (1985) found that $\beta_{\text{eff}} \approx 1.08$ based on (6) and 860 satellite measurements for eight cirrus clouds in a 550 km^2 region over the Pacific, centered at 25°N, 150°E. Parol et al. (1991) showed similar β_{eff} results for a small region of cirrus. Giraud et al. (1997) developed an automated split-window analysis using these AVHRR channels that estimates a maximum value for β_{eff}, using 21 AVHRR images of cirrus during fall over the northern Atlantic and Europe. For cirrus temperatures less than −40°C, the mean upper limit for β_{eff} was about 1.12. At warmer temperatures, β_{eff} was larger, but this is believed to be due to the presence of supercooled liquid water (Giraud et al. 2001) as shown by an analysis including Polarization and Directionality of the Earth's Reflectances (POLDER) satellite data where the cloud thermodynamic phase was determined. Therefore, for the cirrus clouds in these studies, β_{eff} from AVHRR appears to have an average value of about 1.08 and a mean maximum value of about 1.12.

While these measurements are considerable in scope, they have two limitations: (i) the more extensive measurements of Giraud et al. (1997) do not yield mean values for β_{eff}, making a climatological estimate of average β_{eff} very uncertain, and (ii) the retrieval equations involve three unknowns (cirrus emissivity ε for two satellite channels and cirrus temperature T) but the two radiance measurements allow only two unknowns to be solved. Hence, in these studies T was approximated as the brightness temperature of the nearest "blackbody" cirrus ($\varepsilon \approx 1.0$).

To address these issues we developed a new retrieval method that solves for T independently of emissivity, using Moderate Resolution Imaging Spectroradiometer (MODIS) carbon dioxide channels. A more detailed description of this method can be found in Mitchell and d'Entremont (2008) and in a future paper. In brief, T is estimated using radiances measured in two CO_2 channels centered at 13.3 and 14.2 μm. The real refractive index here is 1.52 and 1.58 respectively, indicating the absorption contribution from tunneling is almost the same in these channels (Mitchell 2000). The imaginary index n_i is 0.355 and 0.246, respectively, yielding a PSD $\overline{Q}_{\text{abs}} \approx 1.0$ for each wavelength when tunneling is neglected. For these reasons the emissivity in each channel is essentially the same ($\varepsilon_{13.3} = \varepsilon_{14.2}$), allowing us to solve for T using radiance observations from these two channels. Considering their spectral response functions, the MODIS channels used to retrieve β_{eff} were centered at 11.00 and 12.01 μm. The corresponding response function-weighted AVHRR channels are centered at 10.81 and 11.98 μm, making AVHRR β_{eff} slightly greater than MODIS β_{eff}. AVHRR and MODIS β_{eff} values are compared in Heidinger and Pavolonis (2009), although mean values of β_{eff} are not given.

To obtain more extensive sampling of β_{eff}, this method was applied to three case studies: the Tropical Western Pacific International Cirrus Experiment (TWP-ICE) on 2 February 2006 and the Tropical Composition, Cloud and Climate Coupling (TC4) campaign on 22 July and 5 August 2007. The cirrus sampled during these case studies covered approximately 10 428, 65 415, and 41 925 km^2, respectively, based on the approximation of 1 km^2 per MODIS pixel. Since these case studies contained both anvil and in situ cirrus, the mean β_{eff} values obtained should be fairly representative of tropical anvil and in situ cirrus (although it is unclear whether they are representative of cirrus at midlatitudes).

Only single-layer cirrus clouds over ocean were analyzed, making it more straightforward to estimate the clear-atmosphere contribution to the infrared upwelling radiances. These are influenced by two main physical processes: ocean-surface emissivity and atmospheric attenuation. We prescribe ocean-surface emissivity using the model of Nalli et al. (2008), which specifies emissivity as a function of sea surface temperature (SST), wavelength, ocean-surface wind speed, and view angle. The SST analysis is obtained from the National Centers for Environmental Prediction (NCEP) Global Forecast System (GFS) SSTs, which for our case studies are valid within 45 min of the MODIS overpass times. Finally we use the Optimal Spectral Sampling (OSS) model of Moncet et al. (2008) to compute the clear-atmosphere transmittance profiles in the MODIS infrared channels using coincident GFS upper-air temperature and water vapor analyses. With these inputs prescribed, the only unknown left to solve for in a given infrared band is the cirrus emissivity.

Since T was also retrieved, we filtered the retrievals such that (i) $T \leq -35$°C (to insure we were not sampling mixed phase clouds) and (ii) $\varepsilon(11\ \mu\text{m}) \leq 0.40$. The later was done for three reasons: 1) to increase confidence that the satellite radiance observations, and hence the emissivity retrievals, are sensitive to ice particles throughout the entire vertical extent of the cloud, thereby strengthening the relationship between T and cirrus microphysics; 2) thermal radiances are affected strongly by the particle size and shape in thin cirrus but less so as the cirrus become optically thicker (Wendisch et al. 2007), with blackbody cirrus radiances containing no microphysical information ($\beta_{\text{eff}} = 1.0$); 3) β_{eff} retrieval errors due to partial cloud coverage of a pixel are relatively low when $\varepsilon(11\ \mu\text{m}) < 0.5$ (Heidinger and Pavolonis 2009). Results from this analysis are summarized in Figs. 4 and 5. Using all $\varepsilon(11\ \mu\text{m})$ for $T \leq -35$°C, the retrievals were partitioned into nine $\varepsilon(11\ \mu\text{m})$ intervals of width 0.10, with mean values of $\varepsilon(11\ \mu\text{m})$ and β_{eff} calculated within each interval. These are shown in Fig. 4 for each case study, with one standard deviation (σ) from the mean β_{eff} given by the vertical bars. The curves are remarkably similar, suggesting little variance in β_{eff} as a function of $\varepsilon(11\ \mu\text{m})$ as per location and cloud system. This relationship could be due to a relationship between PSD effective diameter D_e and the IWP, where IWP is directly related to $\varepsilon(11\ \mu\text{m})$, or it could result from reason 2 above, or perhaps both factors are responsible. For the three case studies, the mean value of β_{eff} for $\varepsilon(11\ \mu\text{m}) \leq 0.4$ and $T \leq -35$°C is 1.065 ± 0.046. This is the β_{eff} value that all "retrievals" in this paper are based on and, since the PSD schemes are functions of T, a single β_{eff} value assumes that β_{eff} is independent of T. In Fig. 5, β_{eff} is related to T for the 22 July 2008 case study [$\varepsilon(11\ \mu\text{m}) \leq 0.4$, $T \leq -35$°C], where the retrievals were grouped into nine equally spaced temperature intervals to provide mean values and σ in β_{eff}. Figure 5 indicates that β_{eff} is independent of T for this case study. The same result was found for the 5 August TC4 case study, and the TWP-ICE case study did not have a sufficient range in T to draw any conclusions. The maximum β_{eff} values reported in Giraud et al. (1997) for $T < -35$°C also indicate β_{eff} is independent of T. Thus, it appears that β_{eff} for cirrus is generally independent of T.

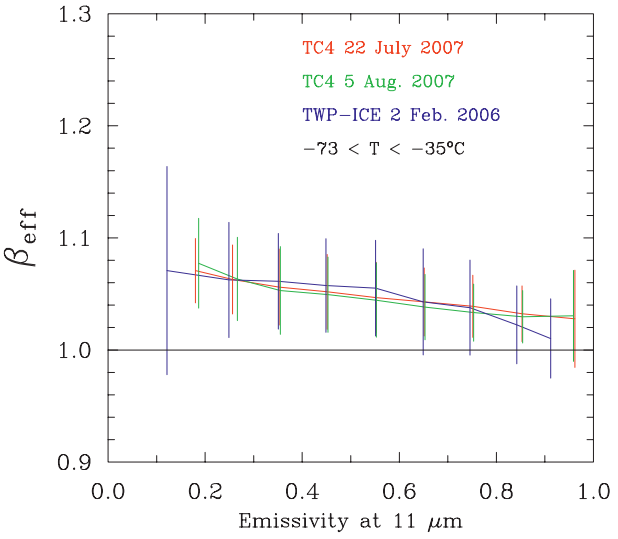

FIG. 4. The mean values of the retrieved effective absorption optical depth ratio β_{eff} related to retrieved mean emissivity for the three case studies with retrieved cirrus temperature <-35°C to insure the clouds are only ice phase. Vertical bars indicate standard deviations and the $\beta_{\text{eff}} = 1.0$ line is given for ease of reference.

c. *Retrieval logic*

The higher the small-mode ice mass content (or small-mode number concentration N_{sm}), the larger β_{eff} becomes. This principle is used to determine N_{sm} by matching theory with observations, as described below:

1) The first step when retrieving cloud properties is to begin with a retrieved cloud temperature and a β_{eff} value. For the purposes of this paper, only β_{eff} is needed while temperature is systematically decreased from −20° to −60°C.
2) From this temperature, the PSD scheme yields a rough estimate of the large-mode mean size $\overline{D}$, the small- and large-mode dispersion parameters, and the small-mode mean size. A "first guess" of β_{eff} is calculated using only the large mode for an arbitrary IWC.
3) If the calculated $\beta_{\text{eff}} < 1.065$, the small-mode contribution to the cirrus IWC is incremented until

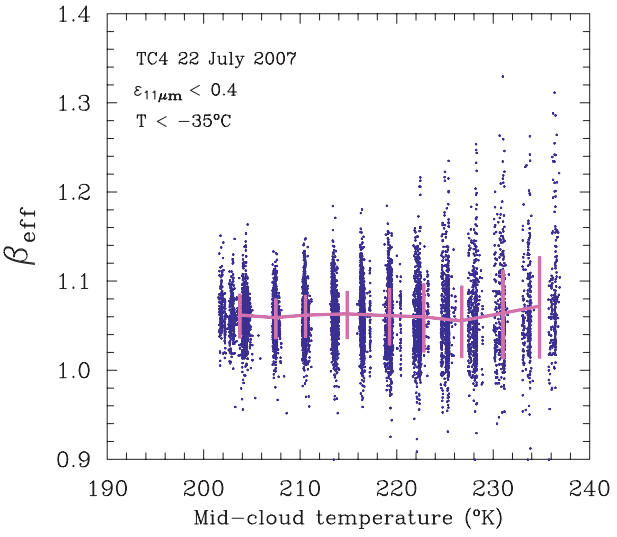

FIG. 5. The retrieved effective absorption optical depth ratio β_{eff} related to cirrus cloud temperature for $\varepsilon(11\ \mu\text{m}) \leq 0.4$ and $T < -35°\text{C}$ using the 22 July 2008 TC4 case study. Mean β_{eff} are given by the pink curve and vertical bars indicate standard deviations.

$\beta_{\text{eff}} = 1.065$. In this case the retrieved large-mode $\overline{D}$ equals the original first-guess large-mode $\overline{D}$.

4) If the calculated $\beta_{\text{eff}} > 1.065$, then no small mode exists, and the large-mode $\overline{D}$ is systematically increased until a match is obtained.
5) In this way the effective diameter D_e and the small-to-larger ice particle concentration ratio $N_{\text{sm}}/N_{\text{lg}}$ can be retrieved. For a given IWC, ice particle number concentration N and the complete PSD are retrieved.

This procedure requires a "most likely" value for α and β in the ice particle mass–dimension relationship: $m = \alpha D^{\beta}$. The same is true for the projected area–dimension relationship: $A = \gamma D^{\delta}$. Since we are using MADA to predict the optical properties, ice particle shape is expressed and quantified through these m–D and A–D relationships, with the m–D expression having the greater impact on the retrieval. New instrumentation and methods have provided improved estimates of α, β, γ, and δ for both small and larger ice particles, as described in the appendix, which provided the values used here. Since the m–D and A–D expressions change as a function of D, the incomplete gamma distribution is used when integrating microphysical and optical properties over the PSD, as described in Mitchell (2002). The sensitivity of the retrieval to these parameters is addressed in section 4b.

4. Results and discussion

a. Size distributions

As shown in Figs. 6–8, the above retrieval was performed on the PSD schemes described in Ivanova et al. (2001), Donovan (2003), and the appendix regarding midlatitude synoptic cirrus; in Heymsfield (2003) and Ivanova (2004) regarding tropical anvil cirrus; and in Schmitt and Heymsfield (2009) regarding tropical tropopause cirrus. The appendix describes a new PSD parameterization method, which has been developed using data from Lawson et al. (2006a) collected from synoptic cirrus. This PSD scheme differs from others in that the large mode is parameterized by considering the entire measured PSD, possibly leading to a more realistic PSD shape. Henceforth this PSD scheme will be referred to as the Mitchell scheme. Ivanova (2004) is based on PSDs sampled during the Central Equatorial Pacific Experiment (CEPEX), henceforth referred to as the CEPEX scheme. With the exception of the Donovan (2003), Heymsfield (2003), and Schmitt and Heymsfield (2009) studies, ice crystals less than 50 μm were sampled by an FSSP, while larger ice particles were sampled by a 2D-C probe. A Cloud Particle Imager (CPI) was used for the Lawson et al. (2006a) dataset for intermediate sizes (characterizing the transition between the FSSP and 2D-C). The novel Donovan PSD scheme is based on ground-based lidar and radar retrievals, although some a priori microphysical information used in the retrieval is based on in situ measurements.

The above retrieval was applied to all PSD schemes using two values of β_{eff}: 1.065 to represent the average or climatological PSD for a given temperature and 1.11 (mean $\beta_{\text{eff}} + \sigma$) to illustrate PSD behavior for one standard deviation σ above the mean β_{eff}. Using the methodology described in the previous section, the PSD was retrieved for each of these PSD schemes for three temperatures, as shown in Fig. 6. The solid curves correspond to $\beta_{\text{eff}} = 1.065$ while the dashed curves correspond to $\beta_{\text{eff}} = 1.11$. The difference between the solid and dashed curves yields an estimate of uncertainty in small ice crystal concentration (only the mean $+\sigma$ concentration is plotted for readability; the mean $-\sigma$ PSD is always monomodal).

These results indicate that the following PSD configurations are consistent with satellite measured radiances at 11 and 12 μm: monomodal superexponential (Mitchell scheme), bimodal exponential (CEPEX scheme), and bimodal subexponential (Ivanova and Donovan schemes), where subexponential refers only to the large mode. There is a slight bimodality for the Mitchell synoptic cirrus at −30°C when $\beta_{\text{eff}} = 1.11$, but otherwise the PSD are superexponential monomodal spectra. The monomodal PSDs are consistent with the radiation since their superexponential attribute introduces many small ice crystals that increase β_{eff}. Nonsuperexponential PSDs require a separate small mode to satisfy β_{eff}. From these results it is difficult to say whether cirrus PSD tend to be

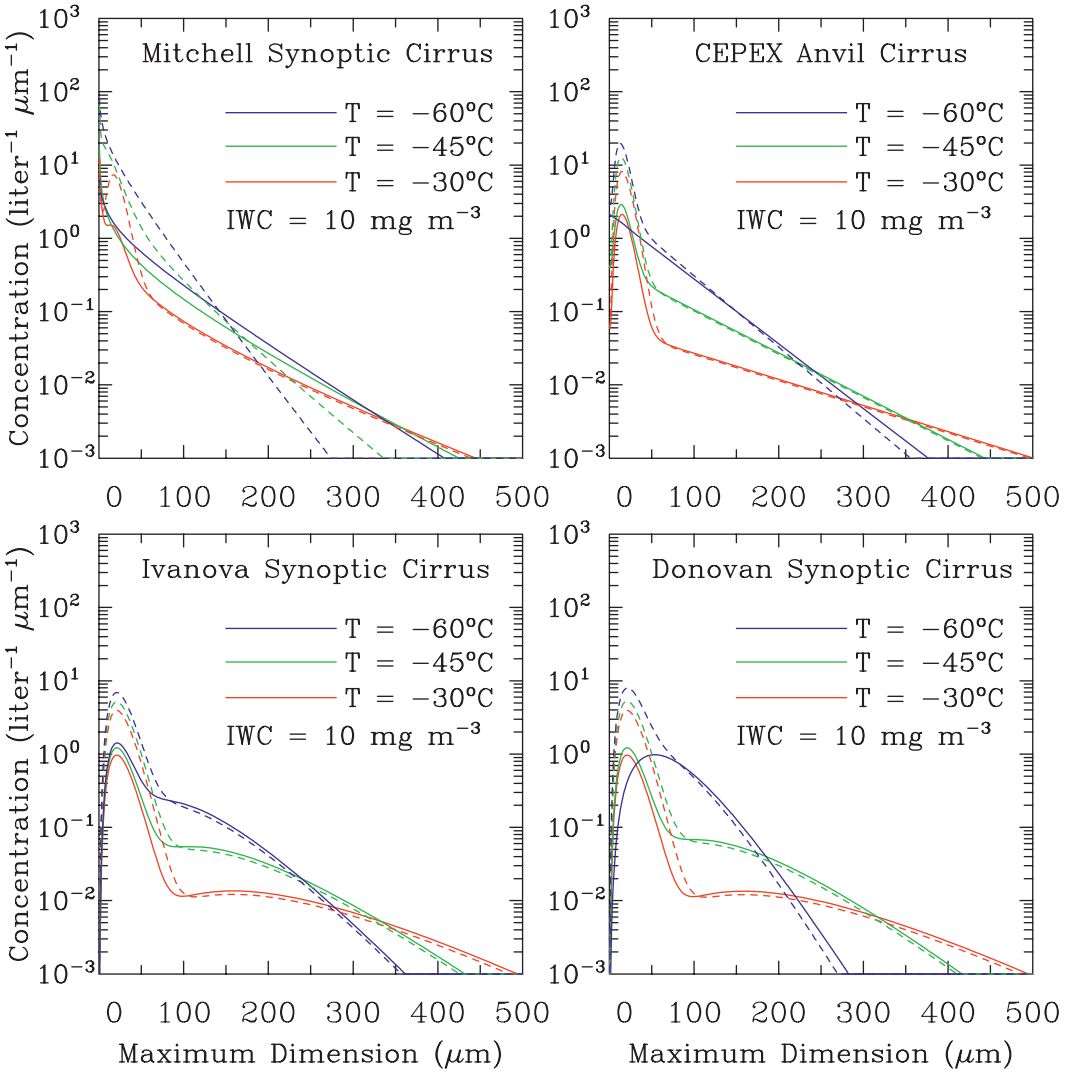

FIG. 6. Retrieved PSD from the indicated PSD schemes based on the mean β_{eff} of 1.065 (solid) and the mean + $\sigma\beta_{\text{eff}}$ of 1.11 (dashed) for the indicated IWC.

monomodal or bimodal. It is possible that the distinction between monomodal and bimodal depends on the methodology employed in parameterizing the PSD. For example, parameterizing the particles measured by the FSSP and 2DC as two separate populations or modes (as done in the CEPEX anvil and Ivanova synoptic schemes) may artificially produce or enhance a bimodal structure. The Mitchell scheme avoids this practice by considering all the particles when parameterizing the large mode (see appendix). There is a clear trend of increasing bimodality with increasing temperature, although this is less apparent with the Mitchell scheme (which exhibits some bimodality at $T = -20$°C).

Figure 7 compares the retrieved climatological PSDs (solid curves) with their corresponding PSD generated by the original PSD scheme (dashed curves). For example, the retrieved PSD at −30°C using a priori microphysics from the Ivanova synoptic scheme (solid red) is compared against the PSD at −30°C predicted by the original Ivanova synoptic cirrus scheme (dashed red). It is seen that the differences between the dashed and solid curves for the Ivanova synoptic scheme are slightly less than the corresponding uncertainty differences reported in Fig. 6. This suggests that the small ice crystal concentrations predicted by the Ivanova et al. (2001) scheme are well within the range of observed concentrations, based on the uncertainty in β_{eff}. For the other PSD schemes, the original scheme overpredicts the concentrations of small ice crystals (relative to the retrieval), often by an order of magnitude or more. A possible explanation is the ice particle shattering phenomena described in the introduction. The Donovan scheme is not based on in

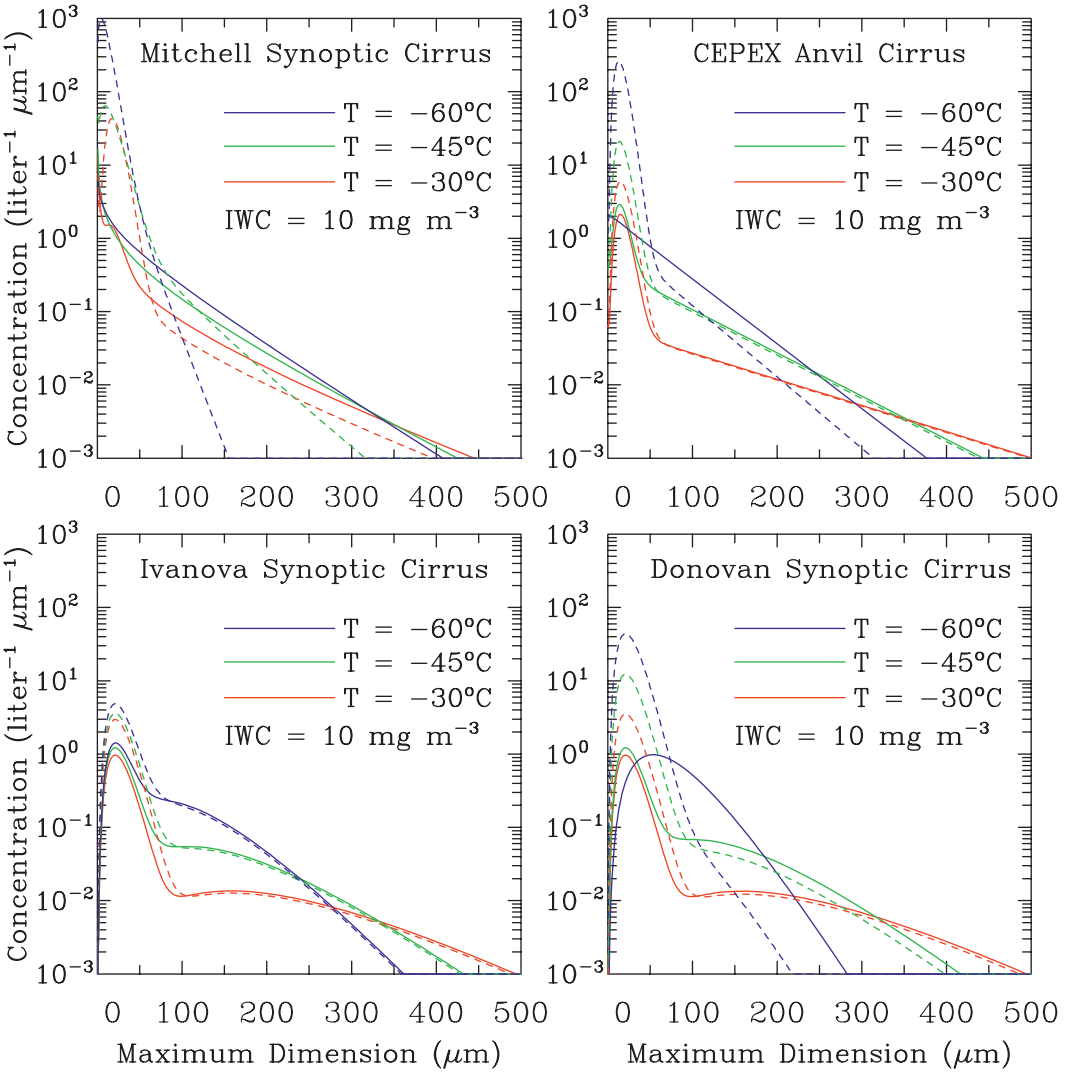

FIG. 7. Retrieved PSD (solid) based on $\beta_{\text{eff}} = 1.065$ compared with the corresponding PSD from the original PSD scheme (dashed).

situ aircraft measurements, so ice particle shattering was not a factor in this study. Overprediction by the Donovan scheme appears greatest at $T = -60$°C, but at $T = -30$°C the Donovan PSD is within the concentration uncertainties shown in Fig. 6.

A possible explanation for the relative agreement between the Ivanova scheme and the Ivanova retrievals in Fig. 7 is that the FSSP-100 used in Ivanova et al. (2001) incorporated a 6-μs "dead time," as suggested in that paper. That is, after a particle was detected and sized, the probe electronics were inactive for 6 μs before another particle could be sized. During this period (corresponding to 600 μm at an airspeed of 100 m s^{-1}), if the detected particle were the leading edge of a cluster of shattered artifacts, most of the trailing artifacts would be ignored as they pass through the sample volume. Other possible explanations may also exist and the cause of this agreement is speculative at this time.

The PSD schemes of Heymsfield (2003) and Schmitt and Heymsfield (2009) are evaluated in Fig. 8. The Heymsfield scheme applies to both midlatitude and tropical anvil cirrus while the Schmitt and Heymsfield (SH) scheme applies only to tropopause cirrus between −56° and −86°C. Since the small ice crystal measurements were not considered reliable in Heymsfield (2003), only ice particle sizes greater than 50 μm were considered. Using a β_{eff} of 1.065, the retrieved PSDs indicate that the concentrations of small ice crystals are underestimated by the monomodal Heymsfield scheme (dashed curves). However, the Heymsfield scheme is consistent with $\beta_{\text{eff}} \sim 1.035$, which lies within one σ of β_{eff}. In general, these retrievals are highly uncertain when $\beta_{\text{eff}} < 1.03$ since

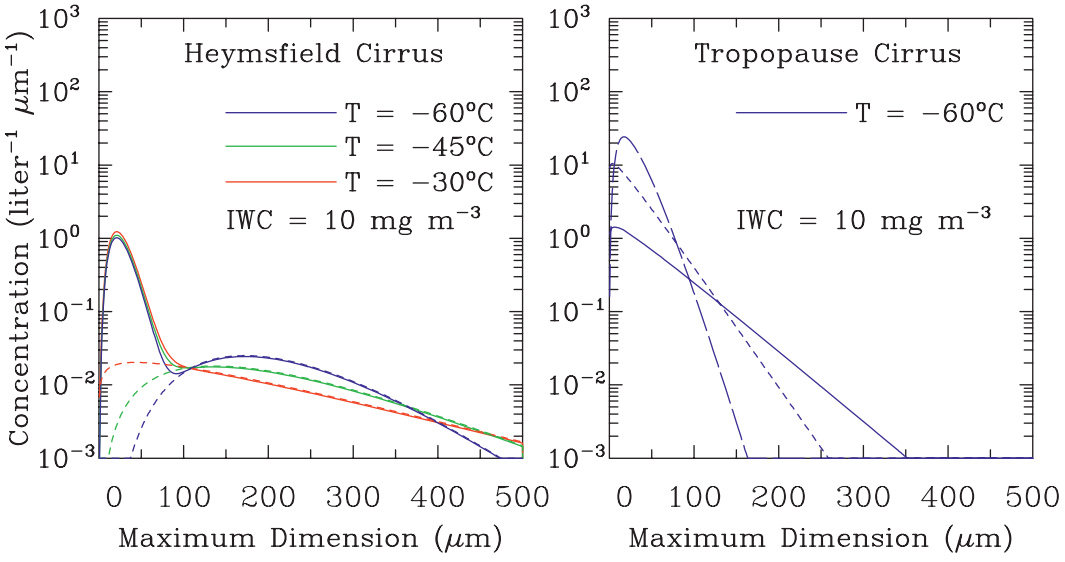

FIG. 8. As in Fig. 7 but for the PSD schemes of (left) Heymsfield and (right) Schmitt and Heymsfield. The long-dashed curve in the right panel is the PSD corresponding to $\beta_{\text{eff}} = 1.11$, one standard deviation above the mean β_{eff} (corresponding to the solid curve). See text for details.

a small change in β_{eff} produces a large change in large-mode $\overline{D}$. The SH scheme (dashed) agrees fairly well with the retrieved PSD (right panel). The long-dashed curve shows the retrieved PSD when based on $\beta_{\text{eff}} = 1.11$ (mean $\beta_{\text{eff}} + \sigma$); the solid curve is for mean β_{eff}. The unmodified SH PSD slope lies between those of the two retrieved PSDs, showing consistency with the retrieved PSDs. The SH scheme is based mostly on VIPS measurements, which accurately measures down to 10-μm particle size. Shattering may be less of a problem for the VIPS since it does not use the inlet tube that characterizes the FSSP and other probes. Finally, the SH comparison illustrates how the retrieval decreases the PSD slope when the initial PSD estimate yields a β_{eff} larger than 1.065 (see section 3c, item 4).

The "radiance corrected" Mitchell scheme exhibits PSDs that appear most similar to PSDs measured with the new two-dimensional stereo (2D-S) probe, where the shattering problem is much reduced. Examples of 2D-S PSDs are shown in Jensen et al. (2009).

b. *Uncertainties*

The retrieved PSDs in Figs. 6–8 depend on the ice particle mass–dimension (m–D) power law assumed. For example, if we use a single m–D expression for bullet rosettes [Eq. (22) in Heymsfield et al. 2002], the retrieved CEPEX PSDs are monomodal for temperatures −40°C and colder. This is because the bullet rosette m–D expression yields lower ice particle masses for a given D than the m–D expressions in the appendix, which translates to a lower effective size D_e. Each PSD ice particle has its own effective size d_e and the tunneling contribution to absorption increases with decreasing d_e. Thus, by decreasing d_e, fewer small ice crystals are required in the PSD retrieval to produce a β_{eff} of 1.065. Owing to the dependence of our PSD results on the m–D expression, we have developed a new method to better characterize an m–D power law for cirrus, as described in the appendix. Since our m–D expressions predict more mass per unit length than many of the m–D expressions in the literature (e.g., Mitchell 1996), our main findings will not be changed by using different m–D expressions. That is, the retrieved PSDs have lower concentrations of small ice crystals than the original PSD schemes predict. Naturally, if the PSD retrievals depend on the m–D expression, so also will the sedimentation velocity V_f and D_e and N, which are derived from the retrieved PSD. Since our m–D expression is supported by measurements from the Counterflow Virtual Impactor (CVI), we feel our estimates for V_f, D_e, and N are realistic. In addition, since the same m–D expression is used for all the PSD schemes considered, relative differences between the retrieved PSDs and the PSD scheme-predicted PSDs should be meaningful (as well as corresponding differences in V_f and D_e).

Reasonable changes in the tunneling efficiency T_e had little effect on the retrieved PSD, V_f, D_e, and N. This is because T_e for small ice crystals is relatively high (Mitchell et al. 2006a) and the tunneling contribution for the larger ice particles is always relatively low (regardless of T_e). For example, regarding the CEPEX PSD, setting the value of T_e to 1.0 for all the small ice crystals

changed V_f and D_e (calculated from retrieved PSD) by less than 1% and 2%, respectively. This change reduced N by up to 13%.

c. PSD sedimentation rates

As noted in the introduction, one of the two factors that most affect climate sensitivity in GCM simulations is the ice fall speed (Sanderson et al. 2008; Mitchell et al. 2008). In this study, we use the ice particle mass and area dimensional relationships developed in the appendix and the radiance-corrected PSD schemes developed in this study to estimate the ice fall speed (that yields the cirrus ice mass sedimentation rate) as a function of temperature. For a given temperature and PSD scheme, the ice fall speed will be calculated from both the original and retrieved PSD.

The relationship between the PSD ice fall velocity and the PSD slope and mass–area dimension power laws will now be described. For a monomodal PSD described by (3), the fall velocity giving the mass flux removal rate from a cirrus layer, V_f, corresponds to the median mass flux dimension or D_f (i.e., the size that divides the PSD mass flux into equal parts). From Ivanova et al. (2001), D_f is defined as

$$D_f = \frac{(\beta + B + \nu + 0.67)}{\lambda}, \tag{7}$$

where B is the power on the fall speed expression

$$V = AD^B. \tag{8}$$

From Eqs. (7) and (12) in Mitchell and Heymsfield (2005), B is given as a function of the Best number X and the mass and area dimensional power laws, where the mass and projected area A_p are given as

$$m = \alpha D^\beta, \tag{9}$$

$$A_p = \gamma D^\sigma, \tag{10}$$

and

$$X = \frac{2\alpha g \rho_a D^{\beta+2-\sigma}}{\gamma \eta^2}, \tag{11}$$

where g is the gravitational constant, η is the dynamic viscosity of air, and ρ_a density of air. The prefactor A in (8), given by (6) and (11) in Mitchell and Heymsfield (2005), is also a function of m–D and A_p–D power laws. To obtain V_f, D_f is substituted into (8), and the mass flux removal rate is simply V_f IWC. It can now be seen that accurate estimates of V_f rely on how accurately the PSD slope λ and the m–D and A_p–D relationships are estimated. It might be noteworthy that ice sedimentation rates are often related to the median mass dimension D_m [$D_m = (\beta + \nu + 0.67)/\lambda$], but it is more accurate to relate them to D_f. For a bimodal PSD, one applies this method to both modes as described in Ivanova et al. (2001):

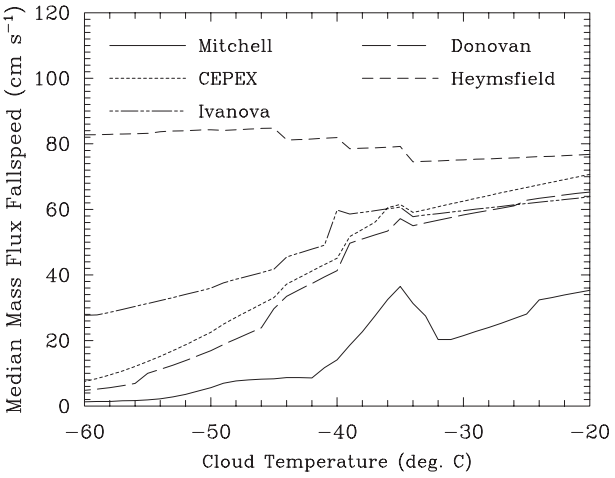

FIG. 9. Temperature dependence of the PSD median mass flux fall velocity for the five applicable PSD schemes that share the same ice particle mass and projected area relationships and standard atmosphere conditions.

$$V_f = (\mathrm{IWC_{sm}}/\mathrm{IWC})V_{f,\mathrm{sm}} + (\mathrm{IWC_{lg}}/\mathrm{IWC})V_{f,\mathrm{lg}}, \tag{12}$$

where subscript "sm" denotes the PSD small mode, "lg" the large mode, and IWC (in the denominator) refers to the total IWC. In the retrieval of small-mode information, the ratio $\mathrm{IWC_{sm}}/\mathrm{IWC}$ is retrieved, which is used in (12).

The results of this analysis are shown in Figs. 9 and 10, where V_f was based on the m–D and A_p–D expressions given in the appendix. Since the treatment of m–D/A_p–D expressions was identical across PSD schemes, differences in V_f can be attributed solely to differences in PSD formulations. Small discontinuities result from the fact that each 5°C interval has a fixed, unique A_p–D expression that abruptly changes between intervals. An m–D expression specific to small ice crystals less than 240 μm ($\alpha = 0.08274, \beta = 2.8135$) and another for larger ice particles ($\alpha = 0.001902, \beta = 1.802$) was used for all temperatures (see appendix). Atmospheric pressure p was estimated for a given temperature T assuming an upper troposphere lapse rate Γ of 7.5°C km^{-1} with $T_o = -20$°C at $p_o = 500$ hPa:

$$p = p_o(T/T_o)^{g/R\Gamma}, \tag{13}$$

where R is the gas constant for dry air and g the gravitational constant.

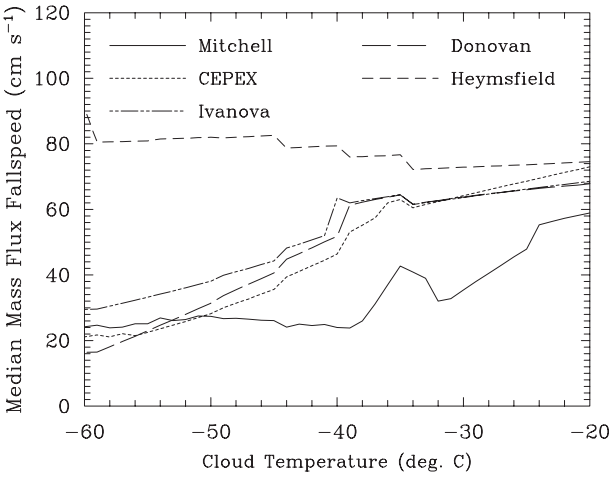

FIG. 10. As in Fig. 9 but fall velocities are based on the retrieved PSD for each PSD scheme.

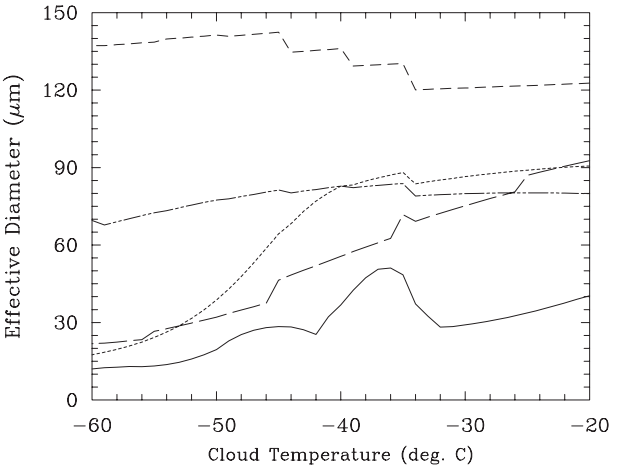

FIG. 11. Temperature dependence of D_e for each of the PSD schemes: all schemes share the same ice particle mass and area assumptions. Legend is as in Fig. 10.

The V_f predicted for the original PSD schemes is shown in Fig. 9 as a function of temperature. The variability in V_f is tremendous, ranging from a few to ~80 cm s^{-1} at low temperatures. The Heymsfield scheme has higher values owing to the absence of small crystals and the PSD shape, resulting in a temperature dependence of λ and ν that causes D_f to increase slightly with decreasing temperature.

Figure 10 shows the same analysis except that V_f is now derived for the retrieved PSD schemes. While β_{eff} is assumed to be constant (1.065) over this entire temperature range, this has been demonstrated only for $T < -35$°C for glaciated conditions (Fig. 5). For the 22 July case at warmer temperatures, β_{eff} slowly increases, probably due to the increasing presence of a liquid phase (Giraud et al. 2001), but mean $\beta_{\text{eff}} \leq 1.10$ for $T \leq -26$°C. This appears consistent with a constant β_{eff} over the range of temperatures plotted here for all-ice conditions.

It is seen in Fig. 10 that, by including the retrieved estimates of the small ice crystal concentrations, the variance in V_f is reduced considerably. However, considerable variance remains, showing the importance of large-mode D_f for predicting V_f. The CEPEX, Ivanova, and Donovan schemes generally yield similar V_f values, consistent with their similar large-mode behavior described in Figs. 6 and 7. For $T < -40$°C, the Donovan and CEPEX schemes exhibit higher V_f than before (sometimes a factor of 2 or more), while V_f for the Mitchell scheme is higher at all temperatures. The Mitchell scheme V_f is roughly constant for $T < -40$°C since the retrieval increases the original $\overline{D}$, producing a quasi-constant $\overline{D}$. In general, V_f is substantially higher in Fig. 10 when the IWC contribution of the small mode is substantially decreased. Since for the Heymsfield scheme the retrieved small-mode IWC was only 4%–5% of the total IWC, V_f for the Heymsfield scheme did not change much. Since the Ivanova small-mode IWC did not change much, V_f did not change much.

In summary, satellite-inferred small ice crystal concentrations may be helpful in reducing V_f uncertainties, but better instruments for in situ PSD measurements are also needed. Some uncertainty is expected owing to natural variability between cloud systems sampled, and information on the type of cirrus (e.g., physical depth, optical depth, anvil, synoptic) may be useful in characterizing V_f. For example, the cirrus reported in Heymsfield (2003) were relatively thick whereas the Lawson et al. (2006a) cirrus were relatively thin.

d. Effective diameter and number concentration

Another cloud property important to climate modeling is the effective diameter or D_e. Here we use the definition of D_e that is universal to both liquid and ice clouds (Mitchell 2002):

$$D_e = 3/2(\text{IWC}/\rho_i P_t), \tag{14}$$

where ρ_i is the bulk density of ice (0.917 g cm^{-3}) and P_t is the PSD projected area. Figure 11 shows the temperature dependence of D_e based on the original five PSD schemes. The legend is the same as for Figs. 9 and 10. Since the m–D and A_p–D expressions are the same as used for V_t and apply to all PSD schemes, differences in D_e are due solely to the PSD differences. Since the Heymsfield scheme is based on $D > 50$ μm, D_e is larger there. But even if that scheme is not considered, D_e can still vary by a factor of 4 (from 15 to 60 μm). Figure 12

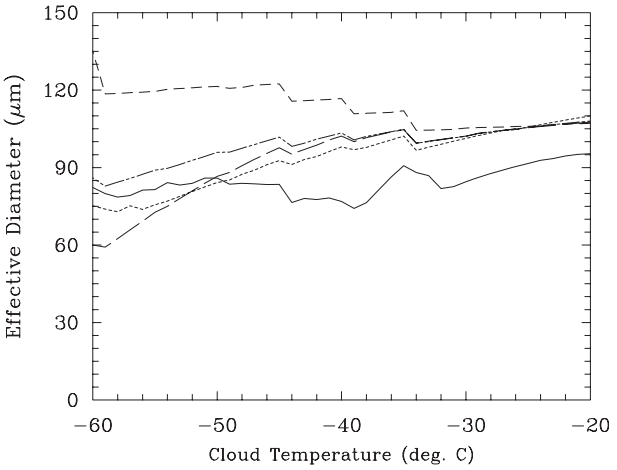

FIG. 12. As in Fig. 11 but D_e is based on the retrieved PSD from each PSD scheme. Legend is as in Fig. 10.

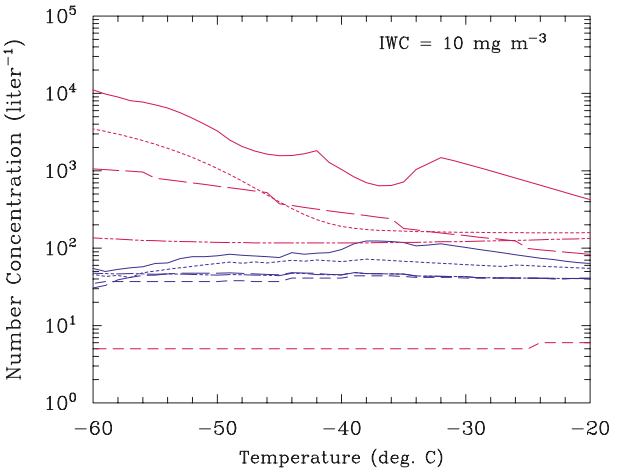

FIG. 13. Temperature dependence of the total number concentration for the original PSD schemes (red) at the indicated IWC and for the corresponding retrieved PSD (blue). For $T > -35$°C the curves for the retrieved Ivanova, Donovan, and Heymsfield schemes are overlaid, with the Ivanova curve only visible around $T = -50$°C. Legend is as in Fig. 10.

examines the temperature dependence of D_e when the five PSD schemes were modified for small crystals based on the retrieval. Although D_e differences for a given temperature are still substantial, the range in D_e values is greatly reduced due to the changes in small ice crystal concentration. These D_e values are larger than many previous estimates (e.g., Francis et al. 1999) because of the m–D expression used, where for $D < 240$ μm, ice particle mass approaches that of a sphere (consistent with the observation of mostly quasi-spherical ice particle shapes). However, these D_e values are typical of those measured during the TC4 experiment where ice artifacts were either greatly reduced or removed from the measured PSD (Jensen et al. 2009).

Using an arbitrary IWC of 10 mg m^{-3}, we contrast the temperature dependence of the number concentration N predicted by the five original PSD schemes with that predicted by the radiance-modified PSD schemes, shown in Fig. 13. The curve legend is the same as in Fig. 10. The N curves given by the modified PSD are colored blue and are clustered in the 40–100 L^{-1} range with virtually no temperature dependence. This concentration range corresponds to the peak in the probability density function for cirrus cloud N sampled during the TC4 experiment (Jensen et al. 2009), where ice artifacts from shattering were minimized or removed. Those curves in Fig. 13 retrieved from the Ivanova and Donovan schemes are overlaid on one another, as is also true for the Heymsfield scheme at warmer temperatures. The N given by the original PSD schemes are in red and lie above these curves, except for the Heymsfield scheme (corresponding to $N \sim 5$ L^{-1}). The Ivanova scheme appears less sensitive to shattering (see also Fig. 7) and the Heymsfield scheme addressed only the larger ice crystals.

If the radiance-modified N curves are representative of nature, this might imply that ice nucleation rates in cirrus clouds are not very dependent on temperature. As temperatures increase, some subset of the nucleated ice crystals might grow more rapidly, producing an ever-broadening large mode and increasing bimodal (or superexponential) appearance (see Fig. 6). More research is needed to verify that the MODIS $\beta_{\text{eff}} \approx 1.065$ at cirrus temperatures, as N here is dominated by the small ice crystals that are largely determined by β_{eff}.

It is not clear why N as given by the original CEPEX, Donovan, and Mitchell schemes increases at the coldest temperatures relative to the corresponding retrieved N. If the N difference (between the original and retrieved PSD) is due to shattering, then this implies that shattering contributions are higher at colder temperatures for which particle sizes are smaller. This finding appears at variance with other studies (Field et al. 2003; McFarquhar et al. 2007; Jensen et al. 2009) that show shattering contributions increase with increasing ice mass and particle size. It is hoped that this paradox will be resolved through future research. It may be noteworthy that the Schmitt and Heymsfield (2009) PSD scheme for thin tropopause cirrus and the Ivanova scheme are not suggestive of enhanced shattering at cold temperatures.

Regarding sampling statistics, the Heymsfield scheme was based on 13 aircraft spiral descents and 3 balloon-borne ascents and the Ivanova scheme was based on 17 flights, while the CEPEX scheme was based on 3 anvil case studies (1 leg-profile per anvil) and the Mitchell

scheme was based on 22 flight missions reported in Lawson et al. (2006a) where the cirrus were relatively thin (mean depth = 1.5 km ± 1.0 km).

The temperature dependence of N in Fig. 13 is broadly consistent with the findings of Gayet et al. (2006) and Krämer et al. (2009), considering that N would decrease with decreasing temperature if IWC did the same. These studies provide reasons why their findings were not significantly affected by the problem of ice particle shattering.

5. Summary

Considerable uncertainty exists regarding the concentrations of small ice crystals ($D < 60$ μm) in cirrus clouds, and their contribution to the PSD may strongly affect GCM predictions of climate sensitivity through their impact on the ice fall speed (Mitchell et al. 2008; Sanderson et al. 2008). The small ice crystals are difficult to measure in situ in part because of the shattering of natural ice particles impacting the inlet tube of the probe used to measure these crystals, thus producing artifacts. Based on a new understanding of the emissivity difference between the 11- and 12-μm channels aboard several satellites, this emissivity difference is used to infer the concentration of small ice crystals for several PSD schemes. This emissivity difference was represented by the 12-to-11-μm absorption optical depth ratio β_{eff}, which was found by several case studies to have a mean value of 1.065 for semitransparent cirrus clouds [$\varepsilon(11\ \mu\text{m}) \leq 0.4$]. Based on this ratio (which appears independent of temperature), a retrieval algorithm was designed to retrieve the small particle mode of the PSD. An existing PSD scheme supplies a priori information to the algorithm, enabling it to estimate the contribution of small ice crystals to the PSD. Combining this small ice crystal estimate with the PSD for larger particles (initially supplied to the retrieval by the original PSD scheme), the complete PSD is obtained. Comparing these retrieved PSD with the original PSD scheme used in the algorithm, the possible impact of ice particle shattering is evaluated for each PSD scheme. Moreover, the retrieved PSD provide new estimates of the temperature dependence of the PSD effective diameter D_e and fall speed V_f for each of the five PSD schemes considered. For a given IWC, the temperature dependence of the ice particle number concentration N was evaluated for each original PSD scheme and its corresponding retrieved PSD.

This analysis revealed that the in situ measurements of small ice crystals do appear to be overestimated (presumably due to shattering), but more so at colder temperatures. However, N from two PSD schemes agreed within one standard deviation of their corresponding retrieved N (Figs. 6, 7, 8, and 13). This study suggests that elevated concentrations of small ice crystals may be real but that their concentrations are generally not as high as some in situ measurements have indicated. However, the spread in our β_{eff} retrievals indicates that cirrus containing high concentrations of small ice crystals ($\sim$1 cm^{-3}) at moderate to low IWPs do sometimes occur. Whether or not the retrieved PSDs are monomodal depends on how the large mode of the PSD is parameterized in the original PSD scheme. If the large mode is parameterized as superexponential, the retrieved PSD tends to be monomodal and superexponential. Otherwise the retrieved PSD tends to be bimodal. The retrieved N was independent of temperature.

If the retrieved PSD is truly representative of natural cirrus, then the uncertainties associated with the temperature dependence of D_e and V_f (as predicted by the original PSD schemes) are reduced considerably for D_e but less so for V_f, based on D_e and V_f from the retrieved PSD. This may be helpful in representing cirrus clouds in GCMs but also underscores the need for improving the treatment of V_f in GCMs. Cirrus radiative properties and climate feedbacks are largely determined through these properties.

Recently there have been instrumentation improvements regarding PSD measurements (e.g., Lawson et al. 2006b; Jensen et al. 2009), and the findings of this study are in general accord with those in Jensen et al. (2009). To have confidence in representing the cirrus PSD in climate models, consistency between in situ and remote PSD measurements is desirable. While Donovan (2003) may have been the first to evaluate the cirrus PSD using ground-based remote sensing, this research effort may be the first to attempt to characterize the cirrus PSD using a satellite remote sensing approach. In this approach, the retrieval infrastructure was derived from in situ measurements of the larger ice particles, and in this way this research can be viewed as a hybrid between remote sensing and in situ measurements. It should be noted that this work did not address Arctic cirrus.

Acknowledgments. This research was sponsored by the Office of Science (BER), U.S. Dept. of Energy, Grant DE-FG02-06ER64201. We also gratefully acknowledge the contributions of John Eylander at the U.S. Air Force Weather Agency for supporting the development of the satellite-based cirrus emissivity retrievals. Comments from the three reviewers of this paper have improved it and are much appreciated. The microphysics retrieval computer codes used in this research are freely available to the scientific community.

APPENDIX

Parameterization of Ice Particle Mass, Area, and Size Distributions Using In Situ Data

This appendix describes the methodology used to develop the Mitchell PSD scheme used in this study. In addition, the ice particle mass–dimension and projected area–dimension power laws used in this study are developed here. Separate power laws apply to the small and larger ice crystals, and these are an important component of the retrieval algorithm.

The aircraft data used to develop this methodology and PSD scheme are described in Lawson et al. (2006a) and consist of 22 flight missions in midlatitude cirrus of nonconvective origin, 104 horizontal flight legs (one PSD per leg), and 15 000 km of in-cloud sampling. The PSDs were measured by the FSSP, CPI, and 2D-C probes over approximate size ranges of 2–30, 31–200, and 201–2000 μm, respectively. These settings varied somewhat between flight missions depending on particle concentrations. Owing to the continuous nature of these PSDs, it was possible to develop this methodology. Although shattering is likely to have produced many small artifact crystals in this dataset (Jensen et al. 2009), it is nonetheless useful for demonstrating and evaluating a new methodology for parameterizing PSD.

The PSD in the Lawson et al. (2006a) midlatitude cirrus dataset can be described as two populations of ice particles. The first population is likely to often be contaminated with shattering artifacts and can be described as a single mode exhibiting a mean maximum dimension $\overline{D}$ between about 10 and 20 μm and extending to sizes of about 60 μm. The second population of ice particles is often observed as a broadened shoulder of the first mode for maximum dimension $D >$ 60 μm for temperatures greater than -50°C. Ice particle morphology changes occurred around an $N(D)$ inflection point near 60 μm, which was selected as the size dividing the two populations for this particular dataset.

a. Analytically describing the PSD

The two populations are parameterized using two gamma functions as defined by (3). The methodology for parameterizing the PSD is similar to that described in Ivanova et al. (2001) but with some improvements. While some PSDs may not require the parameterization of two modes, sometimes PSD are bimodal and this possibility should be allowed for in a parameterization scheme. The two-gamma approach effectively defaults to a single-gamma PSD if there is only one size mode.

The formulas for calculating the gamma distribution parameters when PSD are monomodal (or for the small mode when PSD are bimodal) are as follows:

$$\nu = \frac{[(\beta + 0.67)\overline{D} - D_{\mathrm{m}}]}{(D_{\mathrm{m}} - \overline{D}),} \tag{A1}$$

where β is defined in (9), $\overline{D}$ is the mean maximum dimension, and D_m is the median mass dimension of a given mode. The slope parameter is defined as

$$\lambda = \frac{(\nu + 1)}{\overline{D}} \tag{A2}$$

and the N_o parameter can be defined in terms of N or IWC:

$$N_o = \frac{N\lambda^{\nu+1}}{\Gamma(\nu + 1)} \tag{A3}$$

or

$$N_o = \frac{\lambda^{\beta+\nu+1}\mathrm{IWC}}{\alpha\Gamma(\beta + \nu + 1)}. \tag{A4}$$

To obtain these parameters, ν is first determined from the measured PSD. This requires knowledge of $\overline{D}$, D_m, and β. While the calculation of $\overline{D}$ is straightforward via numerical integration over the measured PSD, the calculation of D_m involves integrating the PSD mass until it matches half of the IWC:

$$\mathrm{IWC}/2 = \sum_{i=1}^{n(D\mathrm{m})} m(D_i)N(D_i)\Delta D_i, \tag{A5}$$

where i refers to PSD bin number, D_i is midpoint of ith bin, ΔD_i is the bin width, and $N(D_i)$ is the ice particle concentration in the ith bin. The IWC is given by the right side of (A5) when the upper limit is the maximum size of the PSD. The calculation of D_m is not sensitive to the choice of α (Mitchell 1991), allowing ν to be determined from (A1). Once ν is determined, λ is calculated from (A2) and N_o can be calculated from (A3) using the measured number concentration N. Alternatively, (A4) can be used if the IWC is measured.

If the PSD are bimodal, the calculation of the large-mode gamma parameters is more involved because the concentrations of the smallest particles in the large-mode gamma distribution are ''masked'' by the small particle mode. Thus, the behavior of the large mode is only partially revealed by the measured PSD. However, ν can be estimated for the large mode by using the entire measured PSD and solving for ν via (A1). But since (A1) is based on $\overline{D}$ and D_m, the largest ice particles in the PSD are not always well represented by the gamma fit. To

remedy this, ν can also be expressed in terms of D_Z—that is, the D that divides the entire PSD into equal parts of radar reflectivity Z:

$$\nu = \frac{[(2\beta + 0.67)\overline{D} - D_Z]}{(D_Z - \overline{D}),} \tag{A6}$$

where D_Z is determined from

$$Z/2 = \sum_{i=1}^{n(D_Z)} [m(D_i)]^2 N(D_i)\Delta D_i \tag{A7}$$

and Z is given by (A7) with maximum size as the summation upper limit (Mitchell et al. 2006b).

For a given gamma function, (A6) yields the same value of ν as (A1) does. However, for measured PSD, (A6) yields a gamma fit having a lower (or more negative) value for ν than does (A1) while better representing the largest ice particle concentrations. Equation (A6) can be derived analogously to (A1) as described in Mitchell (1991).

Once the large-mode ν is determined, the large-mode λ is given by (A2) where $\overline{D}$ and ν correspond to the entire PSD. Neither (A3) nor (A4) can be used to calculate N_o since the number concentration N or the IWC for the large mode is not known (i.e., the contribution of smaller particles to the large-mode gamma distribution fit). However, the large-mode N_o can be determined by solving (3) for N_o:

$$N_o = \frac{N(D)}{[D^\nu \exp(-\lambda D)].} \tag{A8}$$

Using the measured PSD, a point corresponding to the large mode is selected to fix D and $N(D)$ so that N_o can be calculated. In practice, to avoid unrepresentative behavior at a given point, D and $N(D)$ can be averaged over a 5- or 10-micron interval. We now have equations describing all six parameters for the small- and large-mode gamma distributions based on the measured PSD. In section c below we will describe methods of obtaining α and β, thus closing this system of equations and yielding analytical fits to the observed PSD.

b. Parameterizing the PSD

In the approach taken here, the key to parameterizing the PSD in midlatitude cirrus is to first analytically describe the PSD, as described above. Once the various PSD terms are known for each temperature level, the PSD can be diagnosed as a function of temperature and IWC by relating some terms to temperature using polynomial curve fitting. The terms related only to temperature are ν and $\overline{D}$ (for both modes). From these, λ is calculated using (A2). The polynomial best-fit equations are not shown here owing to space limitations.

For bimodal PSD, the two N_o terms can be determined for a given IWC if one knows the ratio of small-mode IWC to total IWC. This ratio can be calculated from the fitted PSD modes using corresponding values for α and β. Then this IWC ratio can be related to temperature using curve-fitting methods. So, for a given temperature and IWC, one knows the IWC in each mode. For example, if the total IWC = IWC_t, the small-mode IWC (IWC_{sm}) is estimated by multiplying the IWC ratio ($\text{IWC}_{\text{sm}}/\text{IWC}_t$) by IWC_t. Similarly, the large-mode IWC is given by the difference $\text{IWC}_t - \text{IWC}_{\text{sm}}$. Knowing the IWC for each mode, N_o for each mode can be estimated by (A4). However, since the small mode includes some particles having $D > 60$ μm and the large mode includes many particles having $D < 60$ μm, and the mass–dimension relationships change across the PSD modes, N_o is most accurately calculated using the incomplete gamma function. This equation for N_o is described in Mitchell [2002; Eq. (A11)].

The PSDs predicted from this parameterization scheme (dashed curves) are compared with the sampling time-weighted mean PSD (solid curves) for each 5°C temperature interval in Fig. A1. The parameterized PSD at the two warmest temperatures are based on an extrapolation scheme using results from Ivanova et al. (2001). Since there are no measured PSD to compare with in these two cases, only the predicted curves are shown. For each temperature interval the midpoint temperature (at which the PSD scheme was evaluated) is indicated, along with the D_e based on the measured and predicted PSD. The measurement-derived IWC was used as input for the PSD scheme.

c. Estimating m–D power laws for cirrus clouds

Little is known about the m–D relationships for cirrus particles as it is difficult to measure in situ the masses of individual ice crystals and to gather meaningful statistics on crystal mass and dimension. However, Baker and Lawson (2006) have developed a method that relates an ice particle's projected area to its mass. Using field measurements of photographed ice crystals and their corresponding melted hemispherical droplet images from which their mass was estimated (described in Mitchell et al. 1990), Baker and Lawson related the projected area of these crystals to their masses. This resulted in m–A_p relationships for calculating the IWC since the A_p directly measured by the optical probes can be translated into particle mass and integrated over the PSD to provide IWC. Figure A2 shows IWCs obtained by applying this technique to 2D-S probe (Lawson et al. 2006b) PSD measurements during the NASA TC4 campaign. As demonstrated in Jensen et al. (2009), the 2D-S measures ice particles from 10 to 1280 μm at jet

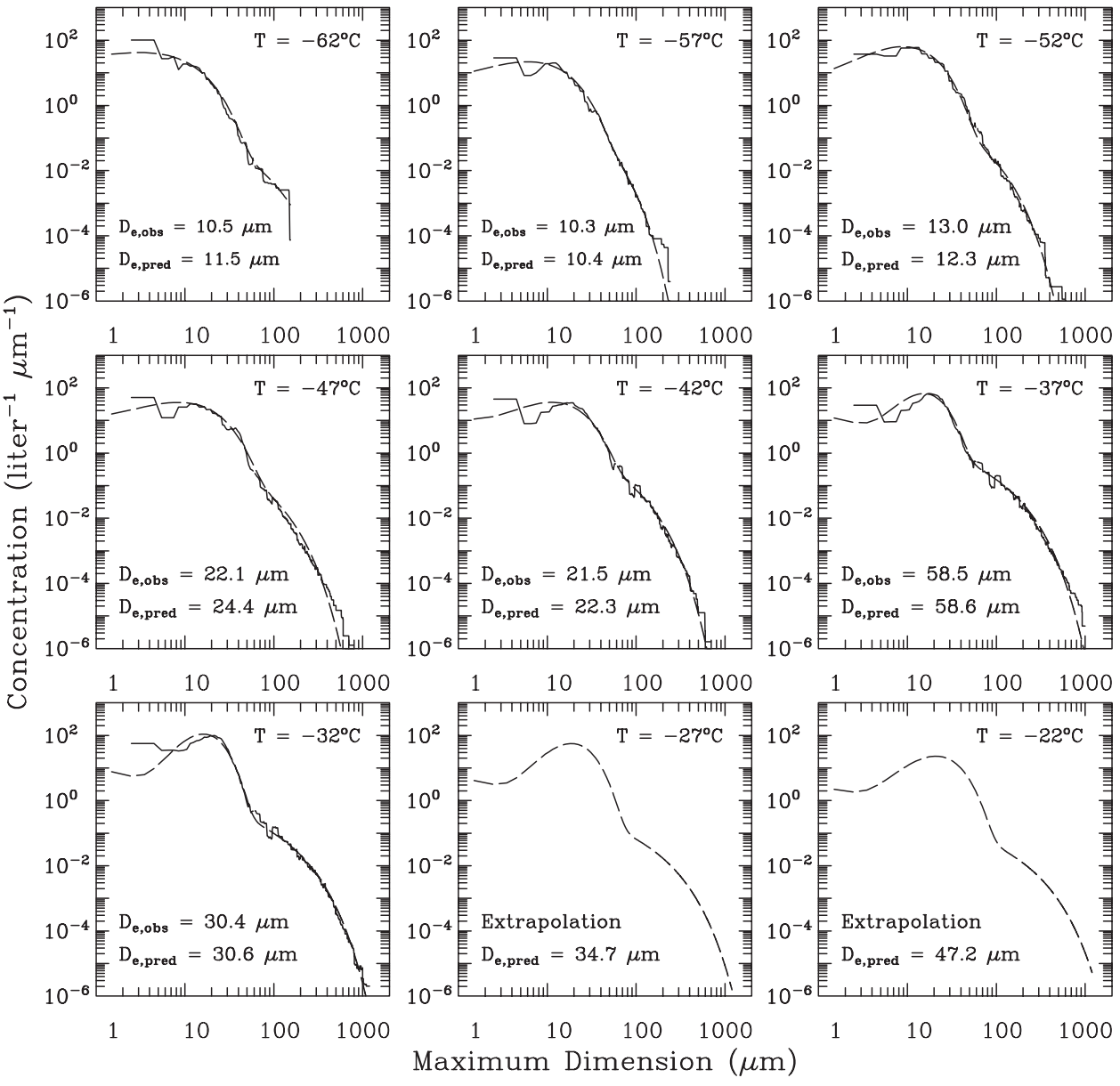

FIG. A1. Comparisons of PSD predicted by the parameterization scheme (dashed) with the time-weighted mean PSD from Lawson et al. (2006a) midlatitude cirrus measurements (solid) for each temperature interval. Note that there are no measurements to compare with the −27° and −22°C parameterizations. Measurement-derived and predicted D_e are compared to evaluate the accuracy of the analytical fits and parameterization procedure.

aircraft speed and electronically processes these measurements using interarrival times to remove shattered particles. These 2D-S IWCs are compared with IWCs measured simultaneously by the collocated counterflow virtual impactor aboard the DC-8. Given that these are two very different methods for estimating the IWC, the agreement is quite good (within ~20% usually). The CVI uncertainty in IWC is estimated to be 13% at water contents of 0.05 to 1.0 g m^{-3} and increases to 16% at 0.01 g m^{-3} and to 40% at 0.0025 g m^{-3} (Heymsfield et al. 2007; Twohy et al. 1997, 2003). The data in Fig. A2b are from all flights in anvil and aged anvil cirrus during the TC4 campaign (covering ~2600 km). Regions of CVI data where the CVI saturates have been eliminated. The CVI saturated between 0.5 and 1.0 g m^{-3}, depending on how the operator set the flow rate. Also, regions where the CVI shows nonzero IWC after exiting cloud (due to residual moisture in the CVI chamber) have been set to zero in Fig. A2b. Figure A2a shows such regions where the blue 2D-S curve is at zero (no cloud),

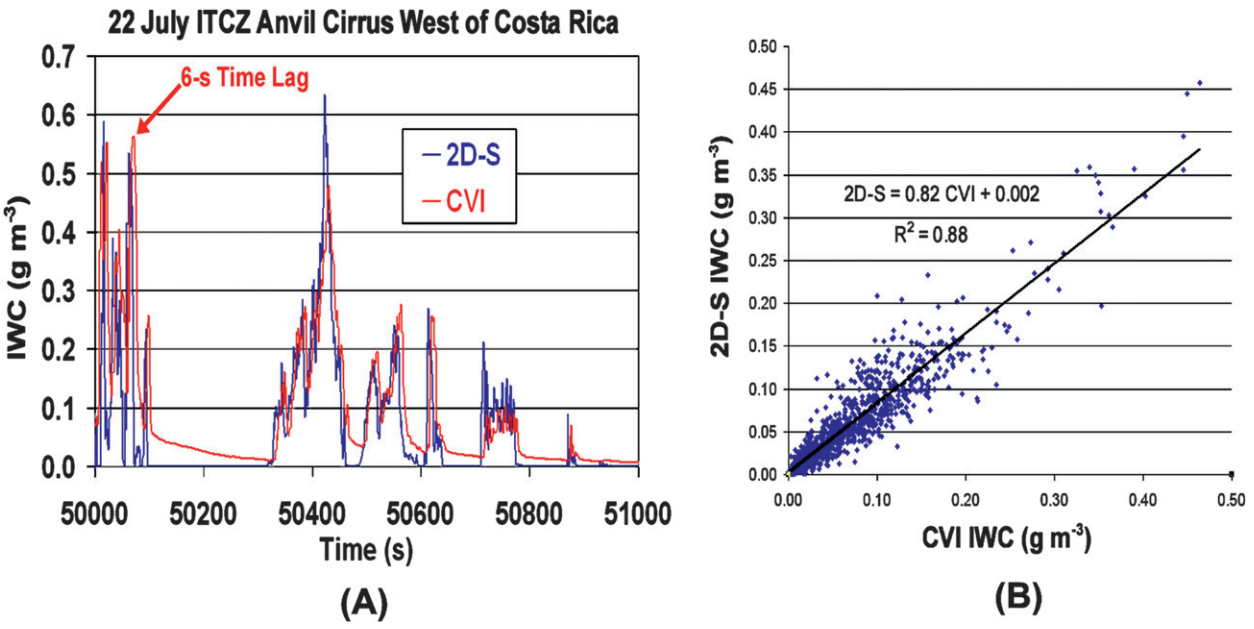

FIG. A2. (a) Time series of the 2D-S and CVI IWC for a TC4 case study. CVI response time lagged 6 s behind 2D-S measurements, producing a slight offset. (b) 2D-S IWCs compared with CVI IWCs for 12 000 1-Hz measurements (averaged over 10 s) in TC4 anvils cirrus.

while the red CVI curve is nonzero. This agreement between the CVI and 2D-S IWC provides some level of confidence that the 2D-S IWCs are realistic. It should be noted that Heymsfield et al. (2002) also found that ice particle area was a better predictor of mass than ice particle maximum dimension.

The 2D-S measurements combined with the m–A_p relationships provide estimates of differential mass concentration in each size bin of the 2D-S, and integrating over the PSD yields the IWC. Dividing the bin mass concentration by the bin number concentration yields the average ice particle mass for that bin. Figure A3 plots for a given PSD the bin average ice particle mass against the bin size midpoint (i.e., approximate average ice particle length in bin), generating m–D relationships for the various PSD. The red curve represents an average of all the PSDs sampled in aged anvils that were generally characterized by dense quasi-spherical particles (classified as spheres or irregulars). The blue curve corresponds to PSD, sampled at the top of an aged anvil at −58°C, comprising almost entirely quasi-spherical particles. As expected, it conforms closely to the dashed black line that gives the m–D relationship for ice spheres. The purple curve is from PSD measured in nonanvil (in situ) cirrus having relatively high bullet rosette concentrations (~20% of total and 50%–60% of the larger ice particles). Surprisingly, the purple curve is not too different from the other curves characterized by dense, blocky, or quasi-spherical ice particles. The black lines are the best-fit lines for the averaged PSD (red curve). The two black lines meet at a size D of 240 μm that seems to divide the PSD into two ice particle shape regimes.

The above illustrates how 2D-S estimates of size-resolved mass and number concentration can be used to produce m–D expressions that yield IWCs similar to those measured by the CVI. This consistency provides added confidence that these m–D expressions are realistic. From the 2D-S PSD data, two m–D expressions are estimated for aged anvil cirrus (red curve), one for $D < 240$ μm:

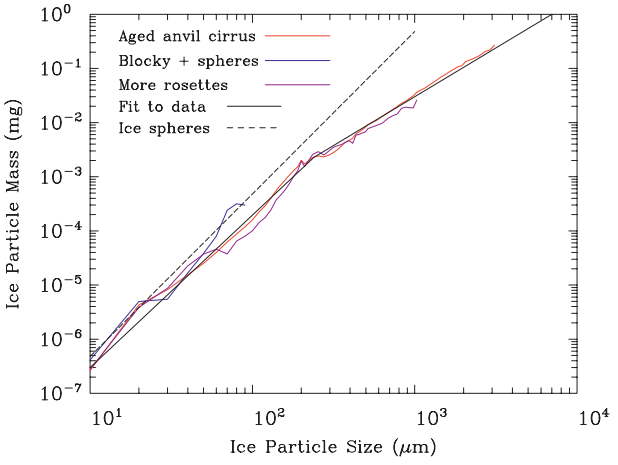

FIG. A3. The m–D relationships derived from 2D-S PSD measurements as described in the appendix.

TABLE A1. Ice particle projected area–dimension power law relationships for each PSD mode and temperature interval.

Temperature interval	Small particle mode		Large particle mode	
	Prefactor	Power	Prefactor	Power
−30° to −35°C	0.4205	1.902	0.1774	1.712
−35° to −40°C	0.2890	1.843	0.1447	1.676
−40° to −45°C	0.3991	1.896	0.1118	1.617
−45° to −50°C	0.4791	1.924	0.099 07	1.600
−50° to −55°C	0.5081	1.933	0.1087	1.628
−55° to −60°C	0.5068	1.932	0.1248	1.665
−60° to −65°C	0.4565	1.914	0.058 69	1.499

$$m = 0.08274\ D^{2.814}, \tag{A9}$$

and one for $D > 240$ μm:

$$m = 0.001902\ D^{1.802}, \tag{A10}$$

where all units are cgs. These expressions were used exclusively in this study. Previous studies (e.g., Heymsfield et al. 2007) have also related m–D expressions to CVI measurements but only a single m–D expression was used to characterize the PSD. As a result of this, ice particles having $D < \sim 100$ μm generally have predicted masses greater than those of an ice sphere of the same length, which is nonphysical. While one can prevent the particle mass from exceeding that of an ice sphere in numerical integrations, it is more practical and accurate to use the incomplete gamma function to perform the integration analytically using two m–D expressions. Near cloud top, maximum particle size is often around 100–300 μm, making a two-m–D approach a must.

In the future we intend to develop temperature-dependent m–D expressions for other types of cirrus, but (A9) and (A10) are sufficient for the purpose of this study.

d. Estimating A_p–D power laws for cirrus clouds

Ice particle projected area–dimension (A–D) power law relationships were developed for this dataset that are representative for each PSD mode at each temperature interval. The CPI renders accurate measurements of ice particle projected area that have been used to determine A_p–D relationships for each PSD mode at each temperature interval. When the PSD projected area for each mode was determined directly from the CPI measurements, the difference between this measured projected area and the projected area calculated by integrating the A_p–D relationships over the PSD was no more than about 3%. The prefactors and exponents for these A_p–D relationships are given in Table A1 as a function of PSD mode and temperature interval, and these relationships were used in this study. Analogous to N_o, the incomplete gamma function can be used for obtaining the highest accuracy when calculating P_t in (14).

REFERENCES

Baker, B., and R. P. Lawson, 2006: Improvement in determination of ice water content from two-dimensional particle imagery. Part I: Image-to-mass relationships. *J. Appl. Meteor. Climatol.,* **45,** 1282–1290.

Baumgardner, D., H. Jonsson, W. Dawson, D. O'Connor, and R. Newton, 2001: The cloud, aerosol and precipitation spectrometer: A new instrument for cloud investigations. *Atmos. Res.,* **59–60,** 251–264.

Donovan, D. P., 2003: Ice-cloud effective particle size parameterization based on combined lidar, radar reflectivity, and mean Doppler velocity measurements. *J. Geophys. Res.,* **108,** 4573, doi:10.1029/2003JD003469.

Downing, H. D., and D. Williams, 1975: Optical constants of water in the infrared. *J. Geophys. Res.,* **80,** 1656–1661.

Field, P. R., R. Wood, P. R. A. Brown, P. H. Kaye, E. Hirst, R. Greenaway, and J. A. Smith, 2003: Ice particle interarrival times measured with a fast FSSP. *J. Atmos. Oceanic Technol.,* **20,** 249–261.

——, A. J. Heymsfield, and A. Bansemer, 2007: Snow size distribution parameterization for midlatitude and tropical ice clouds. *J. Atmos. Sci.,* **64,** 4346–4365.

Francis, P. N., J. S. Foot, and A. J. Baran, 1999: Aircraft measurements of solar and infrared radiative properties of cirrus and their dependence on ice crystal shape. *J. Geophys. Res.,* **104,** 31 685–31 695.

Garrett, T. J., and Coauthors, 2005: Evolution of a Florida cirrus anvil. *J. Atmos. Sci.,* **62,** 2352–2372.

Gayet, J.-F., and Coauthors, 2006: Microphysical and optical properties of midlatitude cirrus clouds observed in the Southern Hemisphere during INCA. *Quart. J. Roy. Meteor. Soc.,* **132,** 2719–2748.

Giraud, V., J. C. Buriez, Y. Fouquart, F. Parol, and G. Seze, 1997: Large-scale analysis of cirrus clouds from AVHRR data: Assessment of both a microphysical index and the cloud-top temperature. *J. Appl. Meteor.,* **36,** 664–674.

——, O. Thouron, J. Reidi, and P. Goloub, 2001: Analysis of direct comparison of cloud top temperature and infrared split window signature against independent retrievals of cloud thermodynamic phase. *Geophys. Res. Lett.,* **28,** 983–986.

Hallett, J., 1976: Measurements of size, concentration and structure of atmospheric particulates by the airborne continuous particle replicator. Air Force Geophysics Laboratory Rep. AFGL-TR-76-0149, 92 pp.

Heidinger, A., and M. J. Pavolonis, 2009: Gazing at cirrus clouds for 25 years through a split window. Part I: Methodology. *J. Appl. Meteor. Climatol.,* **48,** 1100–1116.

Heymsfield, A. J., 2003: Properties of tropical and mid-latitude ice cloud ensembles. Part II: Applications for mesoscale and climate models. *J. Atmos. Sci.,* **60,** 2592–2611.

——, 2007: On measurements of small ice particles in clouds. *Geophys. Res. Lett.,* **34,** L23812, doi:10.1029/2007GL030951.

——, S. Lewis, A. Bansemer, J. Iaquinta, L. M. Miloshevich, M. Kajikawa, C. Twohy, and M. Poellot, 2002: A general approach for deriving the properties of cirrus and stratiform ice cloud properties. *J. Atmos. Sci.,* **59,** 3–29.

——, A. Bansemer, and C. Twohy, 2007: Refinements to ice particle mass dimensional and terminal velocity relationships for

ice clouds. Part I: Temperature dependence. *J. Atmos. Sci.,* **64,** 1047–1067.

Inoue, T., 1985: On the temperature and emissivity determination of semitransparent cirrus clouds by bispectral measurements in the 10-μm window region. *J. Meteor. Soc. Japan,* **63,** 88–98.

Ivanova, D., 2004: Cirrus clouds parameterization for global climate models (GCMs) and North American (Mexican) monsoon modeling study. Ph.D. dissertation, University of Nevada, Reno, 181 pp.

——, D. L. Mitchell, W. P. Arnott, and M. Poellot, 2001: A GCM parameterization for bimodal size spectra and ice mass removal rates in mid-latitude cirrus clouds. *Atmos. Res.,* **59–60,** 89–113.

Jensen, E. J., and Coauthors, 2009: On the importance of small ice crystals in tropical anvil cirrus. *Atmos. Chem. Phys.,* **9,** 5519–5537.

Knollenberg, R. G., 1981: Techniques for probing cloud microstructure. *Clouds: Their Formation, Optical Properties, and Effects,* P.V. Hobbs and A. Deepak, Eds., Academic Press, 15–91.

Korolev, A., and G. A. Isaac, 2003: Roundness and aspect ratios of particles in ice clouds. *J. Atmos. Sci.,* **60,** 1795–1808.

Krämer, M., and Coauthors, 2009: Ice supersaturations and cirrus cloud crystal numbers. *Atmos. Chem. Phys.,* **9,** 3505–3522.

Lawson, R. P., B. Baker, B. Pilson, and Q. Mo, 2006a: In situ observations of the microphysical properties of wave, cirrus, and anvil clouds. Part II: Cirrus clouds. *J. Atmos. Sci.,* **63,** 3186–3203.

——, D. O'Conner, P. Zmarzly, K. Weaver, B. Baker, Q. Mo, and F. Jonnson, 2006b: The 2D-S (stereo) probe: Design and preliminary tests of a new airborne, high-speed, high-resolution particle imaging probe. *J. Atmos. Oceanic Technol.,* **23,** 1462–1477.

McFarquhar, G. M., and A. J. Heymsfield, 1996: Microphysical characteristics of three anvils sampled during the Central Equatorial Pacific Experiment. *J. Atmos. Sci.,* **53,** 2401–2422.

——, and ——, 1997: Parameterization of tropical cirrus ice crystal size distributions and implications for radiation transfer: Results from CEPEX. *J. Atmos. Sci.,* **54,** 2187–2200.

——, J. Um, M. Freer, D. Baumgardner, G. Kok, and G. Mace, 2007: Importance of small ice crystals to cirrus properties: Observations from the Tropical Warm Pool International Cloud Experiment (TWP-ICE). *Geophys. Res. Lett.,* **34,** L13803, doi:10.1029/2007GL029865.

Mitchell, D. L., 1991: Evolution of snow-size spectra in cyclonic storms. Part II: Deviations from the exponential form. *J. Atmos. Sci.,* **48,** 1885–1899.

——, 1996: Use of mass- and area-dimensional power laws for determining precipitation particle terminal velocities. *J. Atmos. Sci.,* **53,** 1710–1723.

——, 2000: Parameterization of the Mie extinction and absorption coefficients for water clouds. *J. Atmos. Sci.,* **57,** 1311–1326.

——, 2002: Effective diameter in radiation transfer: General definition, applications, and limitations. *J. Atmos. Sci.,* **59,** 2330–2346.

——, and W. P. Arnott, 1994: A model predicting the evolution of ice particle size spectra and radiative properties of cirrus clouds. Part II: Dependence of absorption and extinction on ice crystal morphology. *J. Atmos. Sci.,* **51,** 817–832.

——, and A. J. Heymsfield, 2005: Refinements in the treatment of ice particle terminal velocities, highlighting aggregates. *J. Atmos. Sci.,* **62,** 1637–1644.

——, and R. P. d'Entremont, 2008: Satellite remote sensing of small ice crystal concentrations in cirrus clouds. *Proc. 15th Int. Conf. on Clouds and Precipitation,* Cancun, Mexico, ICCP, 185–188.

——, R. Zhang, and R. L. Pitter, 1990: Mass-dimensional relationships for ice particles and the influence of riming on snowfall rates. *J. Appl. Meteor.,* **29,** 153–163.

——, A. Macke, and Y. Liu, 1996: Modeling cirrus clouds. Part II: Treatment of radiative properties. *J. Atmos. Sci.,* **53,** 2967–2988.

——, A. J. Baran, W. P. Arnott, and C. Schmitt, 2006a: Testing and comparing the modified anomalous diffraction approximation. *J. Atmos. Sci.,* **63,** 2948–2962.

——, A. Huggins, and V. Grubisic, 2006b: A new snow growth model with application to radar precipitation estimates. *Atmos. Res.,* **82,** 2–18.

——, P. J. Rasch, D. Ivanova, G. M. McFarquhar, and T. Nousiainen, 2008: Impact of small ice crystal assumptions on ice sedimentation rates in cirrus clouds and GCM simulations. *Geophys. Res. Lett.,* **35,** L09806, doi:10.1029/2008GL033552.

Moncet, J.-L., G. Uymin, A. E. Lipton, and H. E. Snell, 2008: Infrared radiance modeling by optimal spectral sampling. *J. Atmos. Sci.,* **65,** 3917–3934.

Nalli, N. R., P. J. Minnett, and P. van Delst, 2008: Emissivity and reflection model for calculating unpolarized isotropic water surface-leaving radiance in the infrared. I: Theoretical development and calculations. *Appl. Opt.,* **47,** 3701–3721, doi:10.1364/AO.47.003701.

Parol, F., J. C. Buriez, G. Brogniez, and Y. Fouquart, 1991: Information content of AVHRR channels 4 and 5 with respect to the effective radius of cirrus cloud particles. *J. Appl. Meteor.,* **30,** 973–984.

Platt, C. M. R., 1997: A parameterization of the visible extinction coefficient of ice clouds in terms of the ice/water content. *J. Atmos. Sci.,* **54,** 2083–2098.

Ryan, B., 1996: On the global variation of precipitating layer clouds. *Bull. Amer. Meteor. Soc.,* **77,** 53–70.

Sanderson, B. M., C. Piani, W. J. Ingram, D. A. Stone, and M. R. Allen, 2008: Towards constraining climate sensitivity by linear analysis of feedback patterns in thousands of perturbed-physics GCM simulations. *Climate Dyn.,* **30,** 175–190.

Schmitt, C. G., and A. J. Heymsfield, 2009: The size distribution and mass weighted terminal velocity of low-latitude tropopause cirrus crystal populations. *J. Atmos. Sci.,* **66,** 2013–2028.

Twohy, C. H., A. J. Schanot, and W. A. Cooper, 1997: Measurement of condensed water content in liquid and ice clouds using an airborne counterflow virtual impactor. *J. Atmos. Oceanic Technol.,* **14,** 197–202.

——, J. W. Strapp, and M. Wendisch, 2003: Performance of a counterflow virtual impactor in the NASA icing research tunnel. *J. Atmos. Oceanic Technol.,* **20,** 781–790.

Warren, S. G., and R. E. Brandt, 2008: Optical constants of ice from the ultraviolet to the microwave: A revised compilation. *J. Geophys. Res.,* **113,** D14220, doi:10.1029/2007JD009744.

Wendisch, M., P. Yang, and P. Pilewskie, 2007: Effects of ice crystal habit on thermal infrared radiative properties and forcing of cirrus. *J. Geophys. Res.,* **112,** D08201, doi:10.1029/2006JD007899.

Yang, P., H. Wei, H.-L. Huang, B. A. Baum, Y. X. Hu, G. W. Kattawar, M. I. Mishchenko, and Q. Fu, 2005: Scattering and absorption property database for nonspherical ice particles in the near- through far-infrared spectral region. *Appl. Opt.,* **44,** 5512–5523.